Universidade de São Paulo
Instituto de Física

Estudo de métodos analíticos para detecção de traços de elétrons oriundos do decaimento de quarks pesados por colisões pp a $\sqrt{s}$ = 8TeV no ALICE

Marco A. Luzio

Orientador: Prof. Dr. Airton Deppman

Dissertação de mestrado apresentada ao Instituto de Física para obtenção do título de Mestre em Ciências.

Banca Examinadora:

Prof. Dr. Airton Deppman - Orientador (IF-USP)

Prof. Dr. Alexandre Alarcon do Passo Suaide (IF-USP)

Prof. Dr. Tobias Frederico (ITA)

São Paulo

2017

FICHA CATALOGRÁFICA
Preparada pelo Serviço de Biblioteca e Informação
do Instituto de Física da Universidade de São Paulo

Luzio, Marco Aurelio

Estudo de métodos analíticos para detecção de traços de elétrons oriundos do decaimento de quarks pesados gerados por colisões pp √s=8TeV no ALICE / Study of analytical methods for electron track detection from heavy quark decays generated by √s=8TeV pp collisions at ALICE. São Paulo, 2017.

Dissertação (Mestrado) – Universidade de São Paulo. Instituto de Física. Depto. de Física Experimental.

Orientador: Prof. Dr. Airton Deppman

Área de Concentração: Física Nuclear de Altas Energias

Unitermos: 1. LHC; 2. Detetores; 3. Colisões; 4. Hádrons; 5. Elétrons.

USP/IF/SBI-008/2017

University of São Paulo
Physics Institute

Study of analytical methods for electron track detection from heavy quark decays generated by $\sqrt{s}$ = 8TeV pp collisions at ALICE

Marco A. Luzio

Advisor: Prof. Dr. Airton Deppman

Thesis submitted to the Physics Institute of the University of São Paulo in partial fulfillment of the requirements for the degree of Master of Science.

Examining Committee:

Prof. Dr. Airton Deppman - Advisor (IF-USP)

Prof. Dr. Alexandre Alarcon do Passo Suaide (IF-USP)

Prof. Dr. Tobias Frederico (ITA)

São Paulo

2017

Acknowledgements

First and foremost I thank God, with all my heart, for all the love, care and strength granted to me; for giving me guidance and an unshakable sense of self-belief; and for being an endless source of inspiration, determination and encouragement during the roughest of times!

I would like to thank my advisor, Dr. Airton Deppman for his patience and understanding, and for believing in my potential to conduct this research project, giving me the opportunity to work alongside him. I also thank the Physics Institute at the University of São Paulo for opening the doors and allowing me to initiate my pursuit towards successfully achieving my academic career goals.

I must, with a deep sense of gratitude, thank the experts at the Istituto Nazionale di Fisica Nucleare (INFN) - Laboratori Nazionali di Frascati (LNF), who were involved in the tutoring and validation of this research project, particularly to Nicola Bianchi and Pasquale Di Nezza, whose interest, participation, input, and validation were crucial and indispensable for the successful conclusion of this project.

I would also like to thank the fellow graduate students who have helped me somehow, especially Cristiane Jahnke, and her advisor, Dr. Marcelo Munhoz, for their essential elucidation on an important programming step. Availing the opportunity, I thank Dr. Shingo Sakai for his initial tips on how to plot data using AliRoot.

Finally, I am immensely thankful to my awesome parents, Maria da Natividade de Figueiredo Luzio and Ademir Luzio, to whom I dedicate this work, for all their support and motivation throughout this experience.

Resumo

Um estudo do uso dos detectores de tempo de voo (TDV), câmara de projeção de tempo (CPT), e calorímetro eletromagnético (CalEM) do ALICE, visando detectar elétrons e pósitrons $(e^{\pm})$ originados por diferentes fontes, foi realizado. Para atingir os objetivos da pesquisa, dados coletados durante o experimento de colisões próton-próton em 2012 foram utilizados. Com um nível de enegia do centro de mass igual a $\sqrt{s} = 8TeV$, a colisão dos feixes de prótons libera quarks pesados, charm e bottom, com tempo de vida de aproximadamente $\approx 10^{-13}s$ e $\approx 10^{-12}s$, respectivamente. Os $e^{\pm}$ gerados pelo decaimento fraco semileptônico de sabores pesados é de interesse para o estudo dos quarks, portanto, o conceito serviu somente como motivação e incentivo para a pesquisa realizada e descrita nesta dissertação. A introdução de cortes específicos, com a finalidade de parcialmente separar dados coletados nos três detectores, permitiu adquirir entendimento sobre os efeitos do cortes nos resultados. Adicionalmente, em virtude do projeto do TDV não ter sido feito visando separar $e^{\pm}$ oriundos do decaimento dos sabores pesados das demais partículas mais massivas, somente os efeitos gerais de introduzir um corte simples nos valores de β (v/c), foram analisados. Os cortes mais específicos foram somente nos dados detectados pelo CPT e pelo CalEM. Uma combinação de cortes baseados na perda de energia da partícula em função da distância percorrida (dE/dx), com a razão entre a energia e o momento da partícula (E/p), foi adotada para viabilizar o processo de separação, desta forma permitindo a separação dos $e^{\pm}$ das demais partículas, ou seja, dos $\pi^{\pm}$, $K^{\pm}$, and $p/\bar{p}$. A análise foi realizada para valores de momento total das partículas na faixa $0 \leq p \leq 6GeV/c$. Uma comparação dos dados originais com os resultados obtidos pela aplicação do procedimento, indicou um aumento substancial do rendimento e eficiência dos $e^{\pm}$, atingindo valores médios acima de 90% na faixa inteira de momento.

Palavras-Chave: CERN; LHC; ALICE; tempo de voo; câmara de de projeção de tempo, calorímetro eletromagnético; decaimento de sabores pesados; decaimento semileptônico; cortes de dados; equação Bethe-Bloch; colisão próton-próton.

Abstract

A study of the usage of ALICE's time of flight (TOF), time projection chamber (TPC), and electromagnetic calorimeter (EMCal), aiming at detecting and separating electrons and positrons ($e^{\pm}$) originated from different sources, was carried out. To accomplish the objectives of the research, data gathered from the 2012 proton-proton (pp) collision experiment were used. At a center of mass energy of $\sqrt{s} = 8TeV$, the collision of the proton beams liberates heavy quarks, charm and bottom, with approximate lifetimes of $\approx 10^{-13}s$ and $\approx 10^{-12}s$, respectively. The $e^{\pm}$ generated through weak semileptonic heavy flavor decays are of interest for studying quarks, therefore it served solely as motivation and incentive for the research carried out and described herein. The introduction of carefully selected cuts, with the purpose of separating partial data collected in the three detectors, permitted the understanding of their effect on the results. Furthermore, due to the fact that the TOF's design was not meant to separate $e^{\pm}$ from the other heavier particles, only the general effects of introducing a simple cut in the β (v/c) values were analyzed. The more specific cuts were only used for the data generated by the events detected by the TPC and the EMCal. A combination of cuts based on the particles' energy loss as a function of traveled distance (dE/dx), with the ratio of energy to momentum (E/p) of the particle, was adopted to enable the separation process, thus allowing for the isolation of $e^{\pm}$ from the other particles, namely $\pi^{\pm}$, $K^{\pm}$, and $p/\bar{p}$. The analysis was performed for values of total particle momentum in the range $0 \leq p \leq 6GeV/c$. A comparison of the raw data with the results obtained by applying this procedure, indicated a substantial increase in the $e^{\pm}$ yield and efficiency, reaching average values above 90% over the entire momentum range.

Keyword: CERN; LHC; ALICE; Time of Flight; Time Projection Chamber; Electromagnetic Calorimeter; Heavy Flavor Decay; Semileptonic Decay; Data Cuts; Bethe-Bloch Equation; Proton-Proton Collision.

Contents

List of Figures

List of Tables

1 Introduction

Since the advent of particle accelerators and detectors, experimental high energy physics has embarked on an insatiable quest to confirm, or refute, the theoretical predictions of the standard model. After the discovery of the Higgs boson at the Large Hadron Collider (LHC), located at the *Conseil Européen pour la Recherche Nucléaire* (CERN) a.k.a. European Organization for Nuclear Research, basically the final missing piece of the model was put in place. Although the standard model tends to consolidate itself, based on concrete evidence, there remains a lot of details about its particles constituents that remains to be understood. With that in mind, the main idea and motivation behind the development and construction of an experiment such as the "A Large Ion Collider Experiment" (ALICE) is to find out more about the physics of the early universe, where matter made up of elementary mass and force particles are believed to have existed. But in order to understand what was going on in this primordial particle "soup", extreme high energy collisions of more massive particles turned out to be necessary. This is where particle accelerators and detectors come in. More specifically, the the ultra-relativistic heavy ion collisions that take place in the LHC comes to aid the research in this area. One of the main purposes of heavy ion collisions at ALICE is to generate Quantum Chromodynamics (QCD) matter, which is comprised primarily of quarks and also by the strong force carriers, the gluons. Thus commonly known as Quark-Gluon Plasma (QGP), this matter is hot and dense in nature, and is commonly used to study the properties of particle creation, annihilation, and decay in this phase of matter. The applicability of QGP research at ALICE is mainly to examine what existed in the early universe very first few microseconds after the Big Bang. The experiments at the LHC are capable of providing lead-lead (Pb-Pb) collisions at a center of mass energy of 2.76 TeV, an interaction with high enough energy to produce this sought QCD medium.

Although the title of this study might seem pretentious by encompassing the idea of detecting electrons from heavy quarks decay, i.e. charm and bottom, the development of an algorithm that establishes a method to separate electrons exclusively originated form heavy flavor decays, is actually *not* the main focus of this work. Rather, the work focused on the separation of elec-

trons in general from all the other particles by employing specific techniques based on the type of detector being used. By allowing all electrons to be isolated from the remaining particles, is a way to ensure that the electrons resulting from heavy flavor decay will also be present in the sample. Nevertheless, emission of electrons through heavy flavor hadron decay was the main motivation for this study, instead of being the actual object of the study.

Keeping the focus on the object of the study mentioned in the previous paragraph, that is, on the methods to separate *all* electrons form the remaining particles, it is worth to succinctly describe the semileptonic decay of heavy flavor hadrons, since it is the motivation and the incentive of the research. By adopting throughly the semileptonic decay process, a useful probing method is obtained for the study of proton-proton and heavy ion collisions jets. Beside the strong force that holds quarks together in hadrons, mediated by the gluon, there are also electromagnetic and weak force interactions between quarks as shown in figure 1.1. A semileptonic decay is characterized by the decay of a hadron via the weak interaction. During the semileptonic decay, a lepton and its corresponding neutrino are produced, as well as hadrons. For example, in figure 1.1, it is possible to observe a Feynman diagram of the weak semileptonic decay of an anticharm quark. If an D^- meson decays, one possible way for it to happen is for one of its constituents, the anticharm quark (the other is the down quark), to undergo the weak process given by $\bar{c} \rightarrow e^- \bar{\nu} \bar{s}$, where an antistrange quark, and electron and an antineutrino are produced [1]. In general, due to the confinement of the quarks, the decay process that domi-

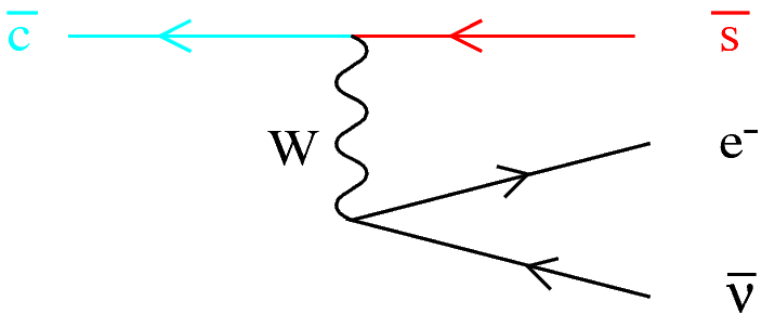

Figure 1.1: Feynman diagram of the a quark's semileptonic weak decay [1].

nates is given by $D^- \rightarrow e^- \bar{\nu}_e K^0$. The neutral kaon, in turn, may semileptonically decay into a positively charged pion, an electron, and the corresponding antineutrino $K^0 \rightarrow e^- \bar{\nu}_e \pi^+$. Figure 1.2 illustrates the transition process from a pseudoscalar heavy meson to a lighter one, which is commonly observed in proton-proton scattering. It is readily possible to note in the diagram that the heavier meson quark decays to a quark that will make up the lighter meson, where in the process an lepton/antilepton and its corresponding neutrino/antineutrino arise via the weak force boson W. Another typical heavy flavor semileptonic meson decay is given by $B^- \rightarrow e^- \bar{\nu}_e D^0$.

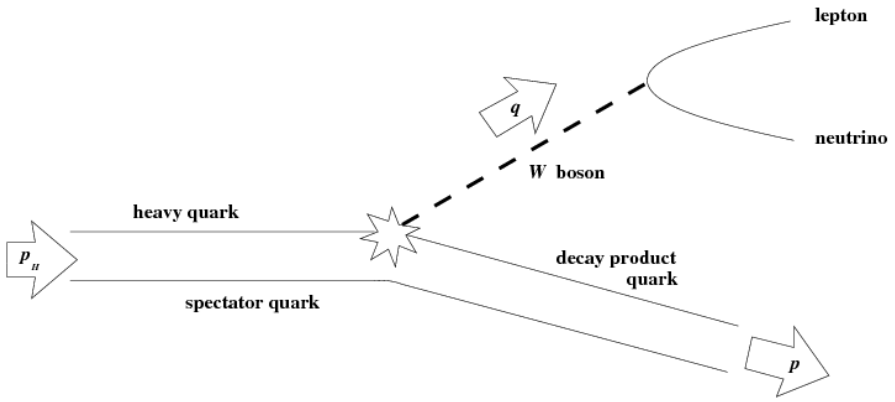

Figure 1.2: This diagram illustrates the pseudoscalar decay of a heavy meson to a lighter meson [2].

The illustration given in figure 1.3 depicts the B^- decay process, going from a heavier meson to a lighter meson while emitting a lepton (e^-) and the corresponding antineutrino in the process. In the diagram it is also possible to note the decay of the bottom to a charm (or up) quark, and the decay of the charm quark to a strange (or down) quark[3].

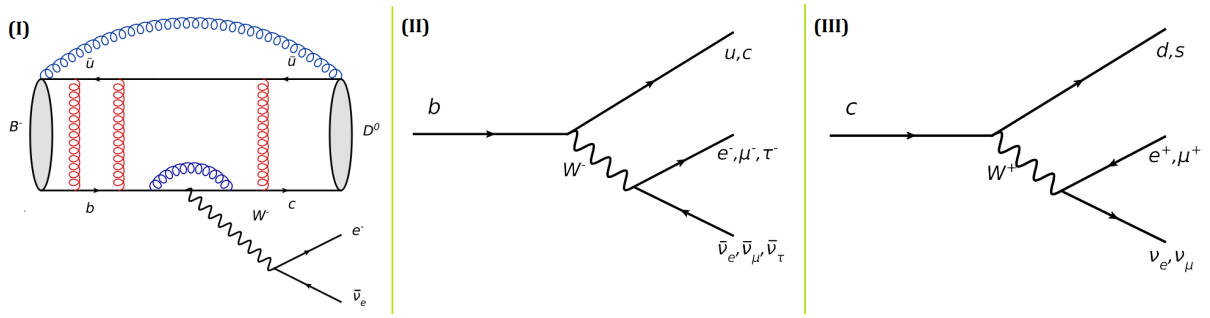

Figure 1.3: This diagram illustrates the semileptonic decay of the (I) B^- heavy meson to a lighter D^0 meson; (II) the decay of the b quark to the $(c;u)$ quark; and (III) the decay of the c quark to the $(s;d)$ quark [3].

Quark mixing is described by an unitary matrix containing parametric information about the lack of correspondence of quantum states. The matrix, denominated Cabibbo–Kobayashi–Maskawa, gives the strengths of the decays that occurs through weak interactions. Basically it specifies the mixing of quark mass eigenstates and weak eigenstates, that is, when quarks propagate freely or when are involved in weak interactions, as couplings between quarks of charge $+\frac{2}{3}$ and quarks of charge $-\frac{1}{3}$ [18, 19, 20]. The matrix is actually given by

$$V_{CKM} = \begin{pmatrix} V_{ud} & V_{us} & V_{ub} \\ V_{cd} & V_{cs} & V_{cb} \\ V_{td} & V_{ts} & V_{tb} \end{pmatrix} \tag{1.1}$$

where each entry each entry V represents the magnitudes, or strength, of the couplings. The

mixing of the three generations of quarks can be obtained by the following matrix multiplication

$$\begin{pmatrix} d' \\ s' \\ b' \end{pmatrix} = V_{CKM} \begin{pmatrix} d \\ s \\ b. \end{pmatrix} \tag{1.2}$$

Parametrizing the V_{CKM} matrix by using three mixing real angles and the complex phase δ responsible for CP-violation, and adopting a widely used standardized convention of symbols, with $s_{kl} = \sin\theta_{kl}$, $c_{kl} = \cos\theta_{kl}$ and δ the phase multiplied by the imaginary number i, V_{CKM} can be written as [**?**, 3]

$$V_{CKM} = \begin{pmatrix} c_{12}c_{13} & s_{12}c_{13} & s_{13}e^{-i\delta} \\ -(s_{12}c_{13}) - (c_{12}s_{23}s_{13})e^{i\delta} & c_{12}c_{23} - s_{12}s_{23}s_{13}e^{i\delta} & s_{23}c_{13} \\ s_{12}s_{23} - c_{12}c_{23}s_{13}e^{i\delta} & -(c_{12}s_{23}) - (s_{12}c_{23}s_{13})e^{i\delta} & c_{23}c_{13} \end{pmatrix} \tag{1.3}$$

Adopting the Wolfenstein approximation, where empirically the ordering in magnitude of the values of s are $1 \gg s_{12} \gg s_{23} \gg s_{12}$, the transformation between mass and weak states, with the matrix entries numerically parametrized, can be written as

$$\begin{pmatrix} d' \\ s' \\ b' \end{pmatrix} = \begin{pmatrix} 1 - \frac{\lambda^2}{2} & \lambda & A\lambda^3(\rho - i\eta) \\ -\lambda & \frac{8(1-\lambda^2)}{2-\lambda^4(1+4A^2)} & A\lambda^2 \\ A\lambda^3(1 - \rho - i\eta) & -A\lambda^2 + A\lambda^4\left[\frac{1}{2} - (\rho + i\eta)\right] & 1 - \frac{A^2\lambda^4}{2} \end{pmatrix} \begin{pmatrix} d \\ s \\ b \end{pmatrix} \tag{1.4}$$

where A, λ, ρ and η are fundamental real constants in the standard model (which shall not be presented here). Because the constant η is multiplied by the imaginary number i, it accounts for all CP-violation phenomena [19].

The last interesting and relevant topic worth introducing, before presenting the actual work, is the interaction of particles with the detector's material. Leptons, hadrons and photon can all be detected by the appropriate detector layer, or module, of the experiment. From the vertex point of interaction, where the beams collide, the produced particles propagate outwards sequentially moving through the different modules, passing through the first component and successively moving on to the adjacent ones. Magnetic fields are applied throughout the various components in order to determine charge and measure momentum by bending the particles' tracks [4]. The tracking systems of experiments such as ALICE, comprised of the Inner Tracking System (ITS), Transition Radiation Detector (TRD) and the Time Projection Chamber (TPC), has as its primary purpose to determine if a particle is charged by determining the sign and the value of such charge, and also calculated the value of the momentum that the particle carries. Moreover, identification of electrons can be achieved by using the data collected at

the electromagnetic calorimeter (EMCal), where the energy of electromagnetically interacting particles, such as the electron, is completely absorbed. The EMCal also determines the amount of energy of the moving particle, and is capable of detecting neutrally charged (null charge) particles. Figure 1.4 depicts the typical arrangement of an experiment's components in its usual modular/sectional configuration. Note that the schematically designed diagram shows four ver-

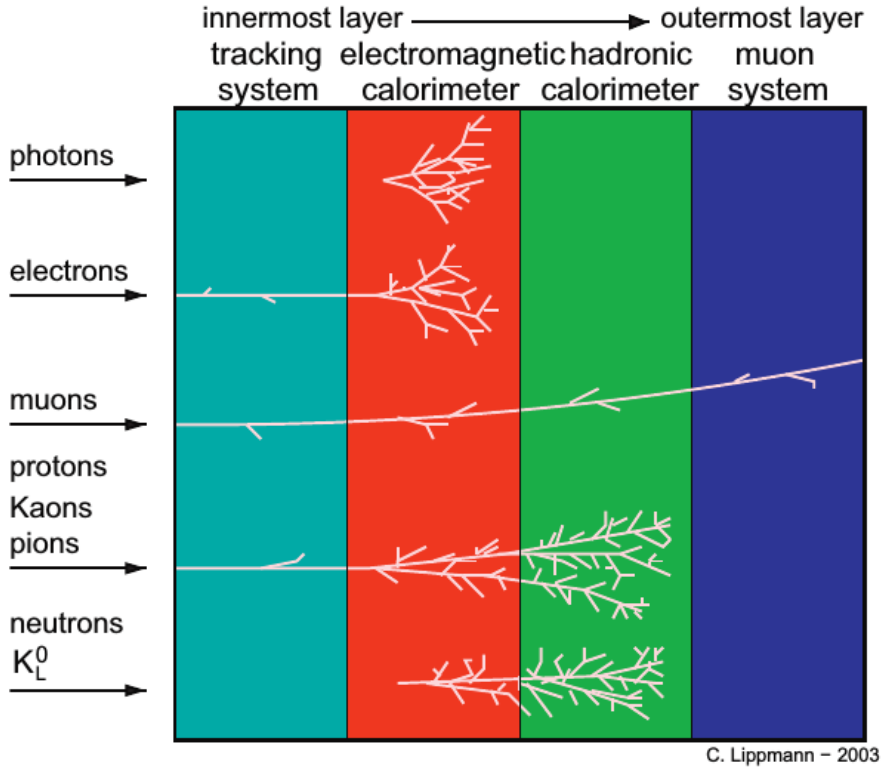

Figure 1.4: Typical layering of particle physics detector components. A detector's suitability for the detection of a particle will depend on the particle's intrinsic characteristics. Some sensitize more than one type of detector, others just one [4].

tical bands, or columns. The first, colored cyan, represents all the components that make up the tracking system. The second, colored red, corresponds to the electromagnetic calorimeter. The third, which is colored green, represents the hadronic calorimeter, and finally the fourth, in the dark blue color, is the muon detection system. For the purposes of the work carried out here, only the first two sections where used. Moving horizontally from left to right though the diagram, is equivalent to the sequence of modules that a particle would encounter after being created. That is, the leftmost column corresponds to the innermost component in the set of detector that comprise the experiment, and the rightmost column to the outermost component.

Analyzing the behavior of different particles as they reach and/or pass through the various modules, it is possible to understand what is expected to be observed in the data. For example, photons (γ) are not readily detectable at the tracking system, but rather deposit all of its energy at the electromagnetic calorimeter. Electrons, on the other hand, are detectable in both sections,

in the tracking system and in the electromagnetic calorimeter. Muons (μ) pass through all the layers leaving the least detectable traces, however, their presence is consolidated in the outer muon system section. Protons and some mesons like the Kaons (K) and pions (π) interact slightly with the electromagnetic calorimeter. Nonetheless these particles deposit all its energetic content in the hadronic calorimeter. Finally, neutrons (n) and the long neutral Kaon $\left(K_L^0\right)$ interact with both calorimeters.

2 *Theoretical Foundations and Analytical Methods*

The fundamental principle underlying the feasibility of conducting an experiment in nuclear or particle physics is that charged particles interact with electromagnetic fields [21]. This concept is at the heart of the theory of beam dynamics and particle accelerator design. Once the particles are accelerated and the collision of the beams take place, the interaction of the produced particles with matter, i.e with the different parts of the detector, allows for the measurement of such particles [22]. Different types of particles behave differently when they come into contact, at high energies, with a particular type of material. Based on this observation, it is thus possible to design and construct instrumentation sensitive enough to detect the specific phenomena that occur during these interactions. The sections presented in this chapter are not the object of study or research, but are basic theoretical principles need to understand how the different detectors operate at a fundamental level.

2.1 High Energy Relativistic Phenomena

Central to the treatment of the results obtained in high energy physics experiments is the fact that particle interactions must obey the laws of special relativity [23]. The high velocities encountered during these experiments oblige the adoption of relativistic considerations during the analytical process. Observables such as momentum and energy, for example, assume different values when compared to the values they would have near the classical velocities, and the physics that takes place in particle accelerators and detectors is almost purely relativistic [21, 23, 24]. The impact of Einstein's theory of special relativity on particle accelerators is crucial for the fully understanding of the phenomena observed in particle detectors after high energy collisions [25], therefore it is worth delineating the main aspects of the theory next.

2.1.1 Four-Vector

To simplify the notation, in relativity it is common to find the symbol $\boldsymbol{\beta}$, which is a dimensionless quantity defined by

$$\boldsymbol{\beta} = \frac{\mathbf{v}}{c}, \tag{2.1}$$

where $\mathbf{v} = \left(v_x, v_y, v_z\right)$ is the three-dimensional vector and c the speed of light in vacuum. This yields

$$\boldsymbol{\beta} = \left(\beta_x, \beta_y, \beta_z\right) = \left(\frac{v_x}{c}, \frac{v_y}{c}, \frac{v_z}{c}\right). \tag{2.2}$$

Lets now consider two inertial reference frames, F and F', where the latter is moving with velocity v_x along the x axis with respect to the former. Assuming these frames reside in Minkowski space, events are then attributed a four component position vector (dependent on the proper time τ) being three the spacial dimensions of the Euclidian space and one associated with time, which can be written as

$$\mathbf{R} = \left(r^0(\tau), \mathbf{r}(\tau)\right) = \left(r^0(\tau), r^1(\tau), r^2(\tau), r^3(\tau)\right) \tag{2.3}$$

where $r^1 = x$, $r^2 = y$, $r^3 = z$, and $r^0 = ct$. This is a position four-vector which upon differentiation with respect to the proper time τ yields a velocity four-vector, which can be expressed as

$$\begin{aligned} \mathbf{V} &= \frac{d\mathbf{R}}{d\tau} \\ &= \frac{d}{d\tau}\left(r^0, r^1, r^2, r^3\right) \\ &= \left(\frac{dr^0}{d\tau}, \frac{dr^1}{d\tau}, \frac{dr^2}{d\tau}, \frac{dr^3}{d\tau}\right) \\ &= \left(v^0, v^1, v^2, v^3\right). \end{aligned} \tag{2.4}$$

For efficiency sake, the velocity four-vector can be conveniently expressed as a linear combination of basis vectors $\mathbf{e}_\mu$ according to

$$\mathbf{V} = \sum_{\mu=0}^{3} v^\mu \mathbf{e}_\mu \tag{2.5}$$

Now, because $r^0 = ct$, it is possible to see that

$$v^0 = \frac{dr^0}{d\tau} = \frac{d(ct)}{d\tau} = c\frac{dt}{d\tau}. \tag{2.6}$$

But it is straight forward to check that $\frac{dt}{d\tau} = \gamma$. The gamma symbol ($\gamma$) is known as the Lorentz Factor and is given by the expression

$$\gamma = \frac{1}{\sqrt{1 - \frac{v_{r1}^2}{c^2}}} = \left(1 - \beta_{r1}^2\right)^{-1/2}. \tag{2.7}$$

Thus it is possible to rewrite the velocity as a four-vector, or *four-velocity*, as

$$\mathbf{V} = \gamma(v)\,(\mathbf{v}, c)\,. \tag{2.8}$$

This intrinsic invariance in the distance separating two events in Minkowsky space-time, naturally applies to an infinitesimal line element ds between two events. By taking the dot product of small changes in $\mathbf{R}$ with itself, the length of squared space-time element is obtained:

$$d\mathbf{R} \cdot d\mathbf{R} = (dr^1)^2 + (dr^2)^2 + (dr^3)^2 - (dr^0)^2 = ds^2. \tag{2.9}$$

A metric tensor $g_{\mu\nu}$ of the Minkowsky space-time can be defined by a four by four symmetric matrix, given by

$$g_{\mu\nu} = \begin{pmatrix} -1 & 0 & 0 & 0 \\ 0 & 1 & 0 & 0 \\ 0 & 0 & 1 & 0 \\ 0 & 0 & 0 & 1 \end{pmatrix} \tag{2.10}$$

So the line element of distance given in equation (2.9) can be written as

$$ds^2 = dr^\mu dr_\mu = g_{\mu\nu} dr^\mu dr^\nu = (d\mathbf{r})^2 - dr^0. \tag{2.11}$$

Here the convention of Einstein's summation notation was used, i.e.

$$g_{\mu\nu} dr^\mu dr^\nu \equiv \sum_{\mu=0}^{3} \sum_{\nu=0}^{3} dr^\mu g_{\mu\nu} dr^\nu \tag{2.12}$$

The coordinates of the moving frame F' can be writen in terms of the coordinates of the rest frame as

$$r'^\mu = \Lambda_\nu^\mu r^\nu. \tag{2.13}$$

where Λ_ν^μ is the usual Lorentz transformation matrix. The Lorentz transformation is an affine linear transformation and it is invariant under translation in the four-dimensional manifold of

space-time [26]. In matrix form the Lorentz transformations on equation (2.9) assume the form

$$\begin{pmatrix} r'^0 \\ r'^1 \\ r'^2 \\ r'^3 \end{pmatrix} = \begin{pmatrix} \gamma & -\beta_{r^1}\gamma & 0 & 0 \\ -\beta_{r^1}\gamma & \gamma & 0 & 0 \\ 0 & 0 & 1 & 0 \\ 0 & 0 & 0 & 1 \end{pmatrix} \begin{pmatrix} r^0 \\ r^1 \\ r^2 \\ r^3 \end{pmatrix} + K \tag{2.14}$$

where K is a constant column vector. Writing it explicitly, one gets

$$\begin{aligned} r'^0 &= \gamma\left(r^0 - \beta_{r^1} r^1\right), \\ r'^1 &= \gamma\left(r^1 - \beta_{r^1} r^0\right), \\ r'^2 &= r^2, \\ r'^3 &= r^3. \end{aligned} \tag{2.15}$$

2.1.2 Energy and Momenta

Two observables of interest in high energy particle physics are the energy and the momentum of the detected particles. These quantities are velocity dependent and can be represented by a single four component vector, defined as the particle's *four-momentum*. The usual relativistic definition of momentum is given by

$$\mathbf{p} = mc\frac{\mathbf{v}}{c\sqrt{1-\frac{v^2}{c^2}}}. \tag{2.16}$$

If the three-dimensional velocity $\mathbf{v}$ is replaced by the four-velocity given in equation (2.8), the four-momentum becomes

$$p^\mu = m\frac{dr^\mu}{d\tau} = \gamma m\frac{dr^\mu}{dt} = \gamma m v^\mu. \tag{2.17}$$

Now, taking into consideration that the v^0 component of the four-velocity is time related, the p^0 component of the four-momentum vector is really the energy of the particle, that is

$$p^\mu = \left(\mathbf{v}, \frac{E}{c}\right). \tag{2.18}$$

Applying the Lorentz transformations to p^μ, it also maps as a four-vector

$$p'^\mu = m\frac{d\left(\Lambda^\mu_\nu r^\nu\right)}{d\tau} = \gamma m\Lambda^\mu_\nu v^\nu = \Lambda^\mu_\nu p^\nu. \tag{2.19}$$

Beside the relations delineated above, the research conducted also uses a relation of energy and momentum to calculate the mass of the detected particles. Taking initially the ration of $p = \gamma m v$

and $E = \gamma mc^2$ [24], we get

$$c\left(\frac{p}{E}\right) = \frac{v}{c}. \tag{2.20}$$

That is, the ratio of momentum to energy yields β and consequently the speed of the particle without the need to calculate the Lorentz factor. Another equation that proved to be useful during the analysis of the data, was the mass calculation based on the relativistic energy and momentum,

$$\begin{aligned} E^2 - (cp)^2 &= \gamma^2 m^2 c^2 \left(c^2 - v^2\right) \\ &= \frac{1}{1 - \frac{v^2}{c^2}} m^2 c^2 \left(c^2 - v^2\right) \\ &= \frac{c^2}{c^2 - v^2} m^2 c^2 \left(c^2 - v^2\right) \\ &= m^2 c^4. \end{aligned} \tag{2.21}$$

So the mass of the particle can be obtained by

$$m = c^{-2}\sqrt{E^2 - c^2 p^2}. \tag{2.22}$$

The particularly useful fact is that the term in the square root is Lorentz invariant, therefore the mass of a particle is observed to be exactly the same in all inertial reference frames.

2.2 Particle Energy Loss

At higher energies, i.e. energies above a threshold of 5MeV, the dominant physical process in the particle-matter interaction is primarily associated with charged particles, which can be detected via the electromagnetic interaction with the electrons of the material that makes up the detector [27]. Substantial differences are observed when charged and uncharged particles traversing through matter. An important feature of charged particles, such as electrons, protons and alpha particles, when compared to neutrally charged particles, such as neutrons and photons, is that the former possesses a mean free path between collisions of only a few Angstroms, whereas for the latter the mean free path ranges in the order of microns to centimeters.

2.2.1 Rate of Energy Loss

Besides relativistic concepts, a rigorous understanding of the energy loss processes comes in handy when dealing with the interactions of particles with matter. Unlike neutrally charged

particles, electrons will loose some energy instantaneously upon entering the material, and will gradually dissipate the remaining energy as it moves through matter leaving a track of a specific range [28]. The velocity and the mass of the scattered particles are very important factors that determine the process by which the particle will loose its kinetic energy while transversing the matter that makes up the detector [22, 23, 27, 29, 30]. Because the focus of the research was on the light leptons, more specifically electrons, generated by the heavy flavor decays, a thorough understanding of the types of interactions that an electron undergoes while traveling through matter is fundamentally important. Higher energy electrons, of about 1MeV, for example, generally leaves a track of length $0.6g/cm^2$ for most materials. On the other hand, electrons with lower energy undergo substantial elastic scattering, which makes its track length considerably shorter [28]. Interactions are mainly characterized by two types of effects, namely energy loss, caused predominantly by the inelastic scattering with the atomic electrons, and path deflection, caused by the elastic scattering with the nuclei. Although these are the dominating reactions, others may occur with less probability, such as Bremsstrahlung and Cherenkov radiation. Inelastic collisions can further be classified as hard and soft. In hard reactions sufficient energy is transfered to the electron, causing ionizations, whereas soft reactions are characterized by just enough energy transfer to result in an excitation state [29]. Although an electron may scatter elastically with basically no energy loss whatsoever [28], the main processes by which energy is given off are described in the next subsections.

2.2.2 Energy Loss by Ionization

To understand how energy is lost in matter, it is interesting to look at the classical derivation of the Bethe-Bloch equation [29, 31, 32, 18]. If particles with total charge equal to Ze, with Z being the atomic number and e the elementary charge, travel with velocity $\mathbf{v}$ towards a stationary electron of an atom that makes up the detector, the interaction will transfer some momentum to the electron. Assuming that the charges are enclosed by cylinder of radius r, where r is the distance of the electron to the central longitudinal axis of the hypothetical cylinder, and with the direction of propagation being along this same axis, the quantity Δp corresponding to the momentum transfer from the incident particles to the electron, is given by

$$\Delta p_\perp = \int F_\perp dt = \int F_\perp \left(\frac{dt}{dl}\right) dl = \int F_\perp v^{-1} dl. \tag{2.23}$$

Note that the only part of the force being considered here is the perpendicular component, because the parallel component cancels out due to the symmetry of the cylinder. Taking then

the perpendicular component of force, which is a function of r, as

$$F_{\perp} = \frac{Ze^2}{l^2+r^2} \cdot \cos\theta = \frac{Ze^2}{l^2+r^2} \cdot \frac{r}{\sqrt{l^2+r^2}}, \tag{2.24}$$

and substituting into equation (2.23), one gets

$$\Delta p_{\perp} = \frac{1}{v}\int_{-\infty}^{\infty} \frac{Ze^2}{l^2+r^2} \cdot \frac{r}{\sqrt{l^2+r^2}} dl = \frac{Ze^2 r}{v}\int_{-\infty}^{\infty} \frac{1}{\left(l^2+r^2\right)^{3/2}} dl. \tag{2.25}$$

Upon integration, the result for the momentum transfer becomes

$$\Delta p_{\perp} = \frac{Ze^2 r}{v}\left[\frac{l}{r^2\sqrt{l^2+r^2}}\right]_{-\infty}^{\infty} = \frac{2Ze^2}{vr}. \tag{2.26}$$

If the energy transfered to a single electron is also considered, it can then be written in terms of the momentum found in equation (2.26) by

$$\Delta E(r) = \frac{\Delta p^2}{2m_e}, \tag{2.27}$$

where r is just the impact parameter. To calculate the energy loss per unit length, one should consider the cylindrical geometry typical of a particle detector. If the electron density per unit volume in a particular material is n, the total number of electrons, N_e in a hollow cylinder of inner radius r, length dl, and thickness dr is just $N_e = n\left(2\pi r \cdot dl \cdot dr\right)$. Therefore, the energy lost for the path length dl and for a distance between r and dr is given by

$$-dE\left(r\right) = \frac{\Delta p^2}{2m_e} N_e. \tag{2.28}$$

Substituting equations (2.26) and (2.27) into equation (2.28), it is possible to rewrite the energy loss expression as

$$-dE\left(r\right) = \frac{4Z^2e^4}{2m_e r^2 v^2} n\left(2\pi r dr dl\right) = \frac{4\pi Z^2 e^4 n}{m_e v^2}\frac{dr}{r} dl. \tag{2.29}$$

After rearranging the terms, it is possible to obtain the rate of energy loss as a function of the distance dl. Integrating the rearranged (2.29) with respect to dr, one gets

$$-\frac{dE}{dl} = \frac{4\pi Z^2 e^4 n}{m_e v^2}\int_{r_{min.}}^{r_{max.}} \frac{dr}{r} = \frac{4\pi Z^2 e^4 n}{m_e v^2} \ln\frac{r_{max}}{r_{min}}. \tag{2.30}$$

The determination of the limits of integration $r_{min.}$ and $r_{max.}$ in (2.30), or of the relevant and realistic range for the impact parameter, can be based on solid physical arguments. Classically arguing these limits, it is straight forward to realize that the maximum transfer of energy happens when the collision occurs head-on. In this situation, the energy gained b the electron is $\frac{1}{2} m_e \left(2v\right)^2$. Relativistically speaking, the energy transfer becomes $2m_e\left(\gamma v\right)^2$, and plugging this

result into equation (2.27), one gets

$$2m_e\left(\gamma v\right)^2 = \frac{2Z^2e^4}{m_e v^2 r_{min.}^2} \rightarrow r_{min.} = \frac{Ze^2}{\gamma m_e v^2}. \tag{2.31}$$

As it is well known, the electrons of the atoms that make up the matter in the detector are bound and revolve around the nuclei with a particular orbital frequency ν. Any perturbation introduced by an incident particle must lie within a shorter period of time τ, where $\tau = \nu^{-1}$. Classically, a common reaction time is $t \simeq \frac{r}{v}$. At higher values of v, relativistic effects must be considered and the time of interaction is given by $t = \frac{r}{\gamma v}$. This implies that $\tau \geq \frac{r}{\gamma v}$ and $\tau = \langle \nu_e \rangle^{-1}$, where the angled brackets indicate the average frequency (ν_e) for all the bound states of the various electrons [29]. So the upper limit of r can be expressed as

$$r_{max} = \gamma \frac{v}{\langle \nu_e \rangle}. \tag{2.32}$$

By substituting the expressions given in equations (2.31) and (2.32) into equation (2.30), the classical Bohr equation for the rate of energy loss is obtained, and can be written as

$$-\frac{dE}{dl} = \frac{4\pi Z^2 e^4 N_e}{m_e c^2 \beta^2} \ln\left(\frac{m_e c^3 \beta^3 \gamma^2}{Ze^2 \langle \nu_e \rangle}\right). \tag{2.33}$$

Another way to approach the limits of the impact parameter r, is that the Heisenberg Uncertainty Principle can be used to find the minimum value of r $(r_{min.})$, that is, the electron must be found within the de Broglie wavelength, or $r_{min.} > \lambda_e$, whereas for the maximum value of r $(r_{max.})$, it is possible to use the fact that the interaction time, given by r/v, must be shorter than the period of the electron, which is γ/ν_e, to ensure proper transfer of energy [31]. On the basis of these arguments, the limits of integration can be written as

$$r_{min.} = \lambda_e = \frac{h}{p} = \frac{2\pi\hbar}{\gamma m_e v}, \tag{2.34}$$

$$r_{max.} = \gamma \frac{v}{\langle \nu_e \rangle} \tag{2.35}$$

By substituting the expressions given in equations (2.34) and (2.35) into equation (2.30), one obtains

$$-\frac{dE}{dl} = \frac{4\pi Z^2 e^4 n}{m_e c^2 \beta^2} \ln\left(\frac{m_e c^2 \beta^2 \gamma^2}{2\pi\hbar \langle \nu_e \rangle}\right). \tag{2.36}$$

where $n = N_A \rho \frac{Z}{A}$ is the electron density, with N_A being Avogadro's number, ρ the density of the medium, Z the charge of the medium, and A the atomic mass of the medium.

Although Bohr approximation contains all the elements and variables necessary to estimate the rate of energy dissipation as a function of distance traveled, it does not taken into consid-

eration the quantum mechanical effects. A corrected equation was derived by Bethe, and other scientists such as Bloch. In this corrected version, the momentum transfer is the parameter used for the derivation, instead of the impact parameter. Also, there usually are two additional corrections considered is this final version, one is a density effect correction and the other is a shell correction. The final equation obtained, a.k.a. Bethe-Bloch Formula, is given by

$$-\frac{dE}{dl} = \frac{4\pi e^4}{c^2 m_e} N_A z^2 \beta^{-2} \frac{Z}{A} \left[\frac{1}{2} ln\left(\frac{2c^2\beta^2 m_e \gamma^2 \Delta E_{max.}}{I^2} \right) - \beta^2 - \frac{\delta}{2} - \frac{C}{Z} \right] \tag{2.37}$$

where I is the ionization potential, $\frac{\delta}{2}$ is the density correction term, $\frac{C}{Z}$ is the shell correction term, and $\Delta E_{max.}$ is the maximum possible energy transfer from the incident particles to the electrons [32], in a single collision, and is given by

$$\Delta E_{max.} = \frac{2m_e c^2 \beta^2 \gamma^2}{1 + \frac{2\gamma m_e}{M} + \left(\frac{m_e}{M}\right)^2}, \tag{2.38}$$

where M is the mass of the nucleus.

For electrons and positrons, the Bethe–Bloch formula shown in equation (2.37) must undergo modification, so that the fact that the incoming particles, i.e. electrons and positrons, have the same mass as the atomic electrons will be taken into consideration [33]. Because the particles are identical, the maximum energy transfer from an electron or positron to an atomic bound electron is equal to half of the value yielded by equation (2.38) [18]. Improving the accuracy of the kinematics, spin and shielding effects, the modified Bethe-Bloch formula for electrons is given by

$$-\frac{dE}{dl} = \frac{4\pi e^4}{c^2 m_e} N_A \beta^{-2} \frac{Z}{A} \left[ln\left(\frac{2c^2\beta^2 m_e \sqrt{\gamma - 1}}{\sqrt{2} I} \right) + \frac{1}{2}\left(1 - \beta^2\right) - \frac{2\gamma - 1}{2\gamma^2} + \frac{1}{16}\left(\frac{\gamma - 1}{\gamma}\right)^2 - \frac{\delta}{2} \right]. \tag{2.39}$$

Although equation 2.39 gives the ionization of atomic electrons due to the incidence of other electrons, it does not take into account an important phenomenon responsible for the energy loss of moving electrons in matter, namely, radiative energy loss due to the emission of photons. This process will be discussed next.

2.2.3 Energy Loss by Radiation

In addition to the energy loss due to ionization, lighter weight particles also loose energy through radiative process. When electrons penetrate the material of the detector, they interact with the Coulomb field of nuclei of atoms. This process causes the particle to slow

down, and the energy lost in the process goes towards emitting photons. This process is called *Bremsstrahlung*, and it happens in experiments that produce particles with energies above the critical level of a few ten's of megaelectron-volts [21, 22, 27, 29, 34, 35, 30]. In other words, the total energy lost by high-energy electrons traveling through a certain medium is the sum of both processes, namely ionization and radiation

$$\left(\frac{dE}{dl}\right)_{Total} = \left(\frac{dE}{dl}\right)_{Ionization} + \left(\frac{dE}{dl}\right)_{Bremsstrahlung} . \tag{2.40}$$

In figure 2.1 one can see the Feynman diagram of the Bremsstrahlung process, where the electron interacts with the Coulomb field of the atomic nuclei.

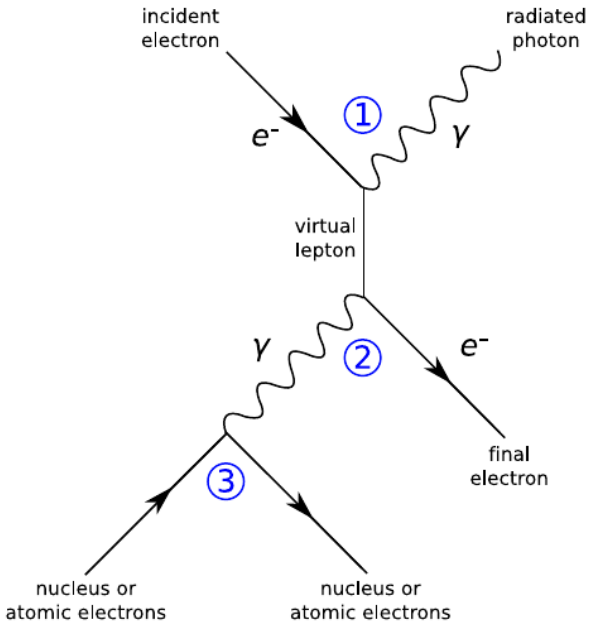

Figure 2.1: Bremsstrahlung Feynman Diagram [5].

The equation that generally describes Bremsstrahlung radiation is

$$-\frac{dE}{dl} = 4\alpha N_A \left(\frac{e^2}{4\pi\epsilon_0 c^2}\right)^2 \frac{Z^2}{A} \ln\frac{183}{Z^{\frac{1}{3}}} \frac{z^2}{m^2} E \tag{2.41}$$

3 *Experimental Apparatus and Data Collection*

3.1 ALICE at LHC

The study carried out used data collected from ALICE, which is comprised of several detectors and parts. However, in this section, a more detail description will be given only to those detectors of the experiment for which the data collected were used to conduct the research described herein. Because the focus was in studying the association of the theoretical predictions with the actual data acquired by the ALICE detectors, data from three main components were used: the TOF, the TPC, and the EMCal.

3.1.1 General Features

When operating to its fullest potential, i.e. at its highest energies, the LHC accelerator has a center of mass energy for pp collisions of $\sqrt{s}$ = 7 TeV and $\sqrt{s}$ = 1.15 PeV for $Pb-Pb$ collisions [36]. The outcome of these collisions can be studied by several detectors, being ALICE one of the main detectors of the LHC. Its main task is to explore the unique physics underlying ultrahigh energy nuclei interactions that occur at the energy levels that LHC is capable of generating. ALICE weighs approximately 10,000 tons and has dimensions of 16m x 16m x 26m, making it occupy a volume of 6,656m^3 [36, 37]. It is made up of two main parts: a central part to measure hadrons, electrons and photons, and a forward spectrometer to measure muons. The central barrel is located inside the outermost (L3) magnet which provides a solenoidal field of up to 0.5T [37, 38]. The pseudorapidity covered by the central tracking detector is in the range of $|\eta| < 0.9$ ($45° < \theta < 135°$) and it covers a full azimuth range [39]. It consists of several parts, the main ones being an inner tracking system (ITS), which consists of six layers of silicon detectors, a time-projection chamber, a single arm electromagnetic calorimeter (PHOS), a time of flight detector, a transition radiation detector (TRD) and a single-arm ring imaging Cherenkov (HMPID) [36, 37, 38]. In addition to these different parts that comprise ALICE, there is also

the important EMCal used in this research. The detector has very good capabilities for heavy flavor measurements. There are several subsystems providing vertex and track reconstruction for high multiplicity events detected at its time projection chamber, which has a maximum detection capability set at eight thousand charged particle per unit of rapidity (dN_{ch}/dy=8,000), commonly given by a $Pb-Pb$ central collision [39]. The quantity rapidity is defined by

$$y = \sqrt{\frac{E+p_z c}{E-p_z c}} = tanh^{-1}\left(\frac{p_z c}{E}\right) \tag{3.1}$$

where E is the energy of the particle, p_z its momentum in the z direction and c the speed of light. Another quantity of interest is the pseudorapidity, a spatial coordinate, defined by

$$\eta = -ln\left(tan\frac{\theta}{2}\right) \tag{3.2}$$

where θ is the angle made by the particle trajectory in relation to the beam axis. It is also capable of identifying particles, such as hadrons, leptons, and photons, distributed throughout a wide momentum range. During these collisions, the temperature can reach up to 200 MeV and the luminosity delivered can reach $10^{27} cm^2/s$, which should not pose a problem since the detector has an upper limit of $10^{30} cm^2/s$ [38, 40]. Figure 3.1 depicts the schematic view of some of the ALICE's subdetectors.

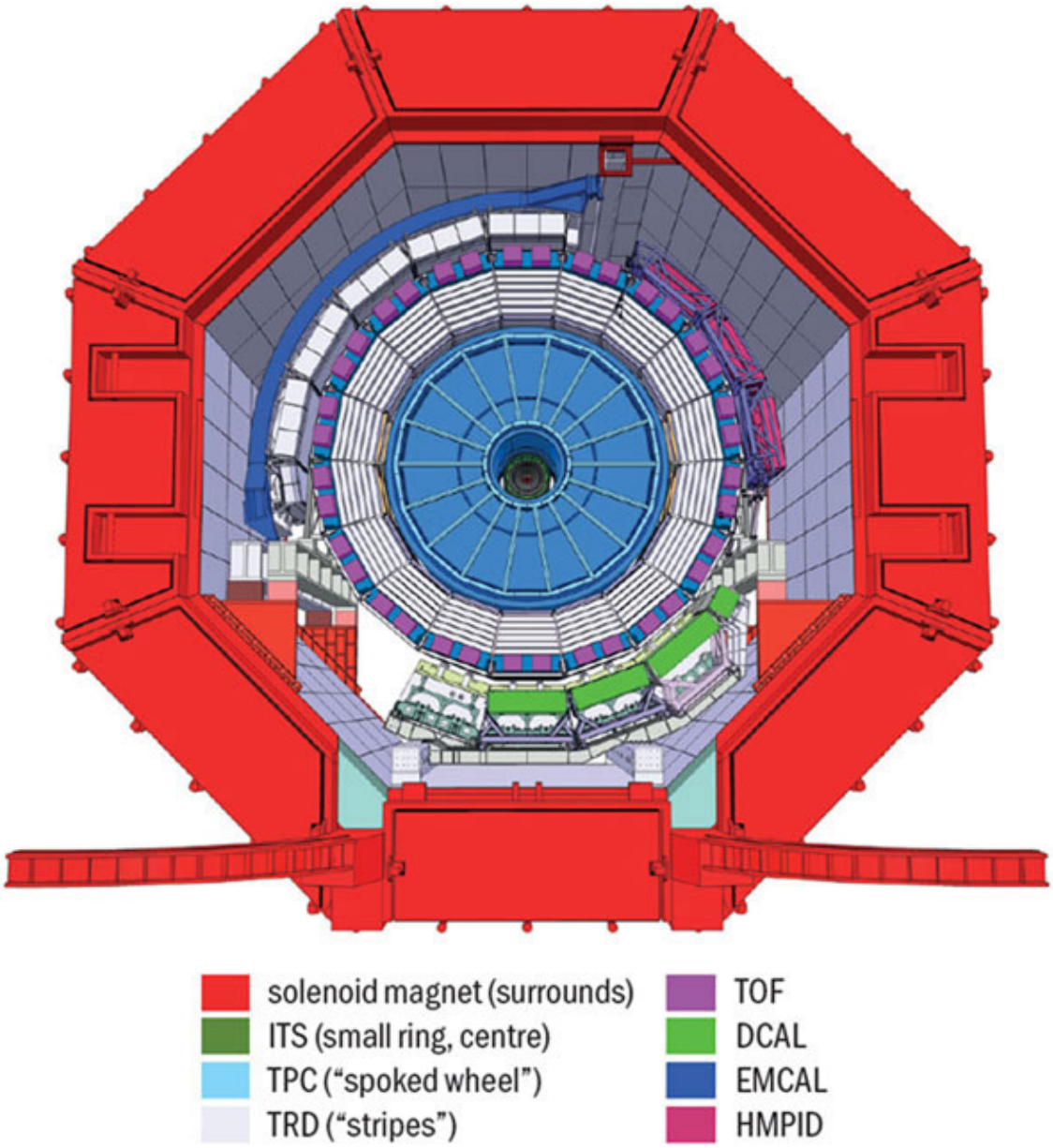

Figure 3.1: A cross section of ALICE showing some of its subdetectors inside the solenoid magnet [6].

3.1.2 Main Chamber

Special attention should be given to the ITS, which is used for the primary and secondary vertex reconstruction. Its two innermost layers are comprised of Silicon Pixel Detectors (SPD) followed by another two layers of Silicon Drift Detectors (SDD). The two outermost layers consist of Silicon Strip Detectors (SSD). Impact parameter resolution of the ITS is of the order of a few hundred microns for very low momentum tracks. It improves with increasing track

momentum and reaches 80 μm at 1 GeV/c. Although the ITS reconstructs the vertices, it is in the TPC where the tracks are initially found, thus the TPC is the main tracking device in ALICE. It provides up to 159 space points per track [40]. The momentum resolution achieved is about 1% for tracks with p_t < 1 GeV/c. Information on the specific energy loss (dE/dx) provided by the TPC is used for particle identification. Provided that there is a sufficient number of hits in the TPC, the track finding efficiency is almost 100% for transverse momentum (p_t) above 0.2 GeV/c. With a magnetic field of 0.5 T, the TPC momentum resolution is about 0.7% at p_t = 1 GeV/c. It has been verified that these performances can be reached at even the highest expected multiplicities of 8,000 charged particles per unit of rapidity [36, 37, 40]. The tracks reconstructed in the TPC are propagated inwards to the ITS. With the ITS, the impact parameter of 1 GeV/c tracks in central $Pb-Pb$ collisions can be measured with a resolution of 50 μm. Due to the lower multiplicity of the pp collisions, this resolution is about 100 μm/in. The ITS is not only important for precision reconstruction of the primary and secondary vertices but also substantially improves the momentum resolution of the TPC at high p_t. Combined tracking in the TRD, TPC and ITS results in a momentum resolution of about 3.5% for p_t = 100 GeV/c and a magnetic field of 0.5 T. The TOF detector extends the PID capabilities of ALICE up to 4 GeV/c [38].

3.1.3 Muon Spectrometer

The second main part that comprising the ALICE detector, namely the muon spectrometer, covers a range of -4.0 < η < -2.5 (171° < θ < 178°) and consists of an arrangement of absorbers, a large dipole magnet and fourteen planes of tracking and triggering chambers. Several smaller detectors are located at forward angles and used for global event characterization and triggering. An array of scintillators is also used to trigger upon the detection of cosmic rays. The two innermost silicon pixel layers of the inner tracking system are used to find the primary collision vertex. In central, high multiplicity, $Pb-Pb$ collisions the vertex is reconstructed with a precision of about 5 μm in the beam direction and about 25 μm in the transverse plane. For pp collisions, with much lower multiplicities, the vertex resolution is worse by about a factor of 10 [36, 37, 38, 40, 41].

3.1.4 Efficiency

The identification of charged hadrons is done by combining the particle identification information provided by the ITS, TPC, TRD, TOF, and HMPID detectors. With the particle abundances expected for 5.5 TeV $Pb-Pb$ collisions, the efficiency of the particle identification

algorithm is found to be above 95% for pions up to about 6 GeV/c, above 60% for Kaons up to 3 GeV/c, and above 70% for protons up to 5 GeV/c. The overall effective particle identification efficiency is limited by particle decays and absorption in the detector material. When integrated over momentum the efficiency is about 50% for pions and protons, and 40% for Kaons. Electrons with momentum above 1 GeV/c are identified by the TRD with an efficiency of more than 90% and with the pion rejection factor of about 100. The track finding efficiency in the muon arm is found to be about 95%. The invariant mass resolution is better than 100 MeV/c^2 which is sufficient to resolve the different quarkonia states. The PHOS spectrometer detects and identifies photons with high energy and position resolution. In the momentum range below $\sim$ 20 GeV/c the direct photon spectrum is obtained from subtraction of the decay photon contribution to the overall identified photon spectrum. These decay contributions are estimated from the measured spectra of light neutral mesons. In the high-momentum range direct photons are identified on an event by event basis by the shower shape and by using isolation-cut discrimination techniques. The identification efficiency for photons with energies $0.5 < E_\gamma < 40$ GeV is above 50% in $Pb-Pb$ collisions and above 90% in pp interactions. The graph in figure 3 depicts the efficiency as a function of transverse momenta for the stand alone TPC and its combination with other parts of the detector. The Photon Multiplicity Detector (PMD) counts photons in the forward rapidity region $2.3 < \eta < 3.5$.

The photon reconstruction efficiency is a function of pseudorapidity with a maximum of about 70% at $\eta = 2.6$. The purity of the PMD photon sample is above 60% in the whole covered range of pseudorapidities. The excellent particle identification capabilities, momentum resolution and complete azimuthal coverage of the central detectors allow comprehensive measurements of particle ratios, momentum spectra, particle correlations, anisotropic flow and event-by-event fluctuations. These observables do not require large amounts of data allowing for further understanding of high-density QCD. The LHC it the first apparatus where heavy quarks are produced abundantly in heavy-ion collisions. Due to the excellent impact parameter resolution and particle identification capabilities, ALICE is well suited to study charm and beauty [38, 42].

3.1.5 Performance

The geometry of the collisions are estimated from the particle energy deposited in the innermost layers of the ITS. Beauty production can be measured from semi-leptonic decays in the range of $2 < p_t < 30$ GeV/c. Single muons and opposite-sign dimuon pairs detected in the muon spectrometer allow for measurements of open-beauty production with high statistics in

the pseudorapidity region -4 < η < -2.5. The measurement of heavy flavor production down to very low transverse momenta is sensitive to the collective motion of heavy quarks in the medium and will provide strong constraints on the thermalization of light quarks. At higher momenta, on the other hand, the measurement of heavy flavor production will provide detailed information on the particle energy loss mechanism. The jet rates in central $Pb-Pb$ collisions at the LHC in the ALICE acceptance are sufficient to map out the energy dependence of jet fragmentation over a wide kinematic range up to $E_t \simeq 200$GeV. Jet reconstruction in nuclear collisions has to cope with the large background from the underlying event, therefore, jet reconstruction has to be limited to a small cone of fixed radius in azimuth and pseudorapidity ranging between 0.3 to 0.5. In addition, a transverse momentum cut in the range 1 to 2 GeV/c has to be applied to reduce the background. As a consequence, even for perfect calorimetry, the transverse energy resolution is limited to $\simeq 20\%$. In its present design, ALICE can measure only the charged particles within the jets, limiting the jet energy resolution to 40 to 50%. Nevertheless, at high E_t, charged jet reconstruction is shown to be much superior for studying high-p_t parton fragmentation compared to using leading particles only, because the bias in the fragmentation function is significantly reduced. The proposed electromagnetic calorimeter for ALICE will improve the jet energy resolution, which further reduces the bias on the jet fragmentation. In addition, it will add a trigger which is needed to increase the statistics at high E_t. Another very promising approach to study jet fragmentation is using prompt photons to tag charged jets emitted in the opposite direction. Prompt photons allow to study the hard interaction without any final state modifications and with this tag the in-medium modification of the fragmentation function will be measured with an accuracy of the order of a few per cent. The combined tracking capabilities of the ALICE detector combined with electromagnetic calorimetry represent an ideal tool for jet structure modifications at the LHC [38, 42].

3.1.6 Impact Parameter

Another interesting and useful feature to look at for the TPC, is the impact parameter projections [7]. For this, it is important to consider the time single track pointing resolution. For transverse momentum values close to $1GeV/c$, this resolution is near $50\mu s$, which is an appropriate resolution value for detecting the electrons originated from the beauty decay, of decay length close to a ten fold factor (about $500\mu s$). By analyzing the reconstructed tracks in the transverse xy plane and longitudinal direction z, the impact parameter, which is defined as the distance of the normal to the path of a projectile to the center of a potential field generated by a

charged particle, is calculated as

$$d_{xy} = qR - q\sqrt{(x_v - x_c)^2 + (y_v - y_c)^2} \tag{3.3}$$

and

$$d_z = z_{track} - z_v. \tag{3.4}$$

where q is the sign of the charged particle, R is the radius of the track projection, (x_c, y_c) are the center coordinates of the track projection (a circle) in the transverse plane, and (x_v, y_v, z_v) is the position of the collision vertex. Figure 3.2 depicts the gaussian distribution on residuals between measured and expected impact parameter for p_T between 0.5 and 0.6 GeV/c.

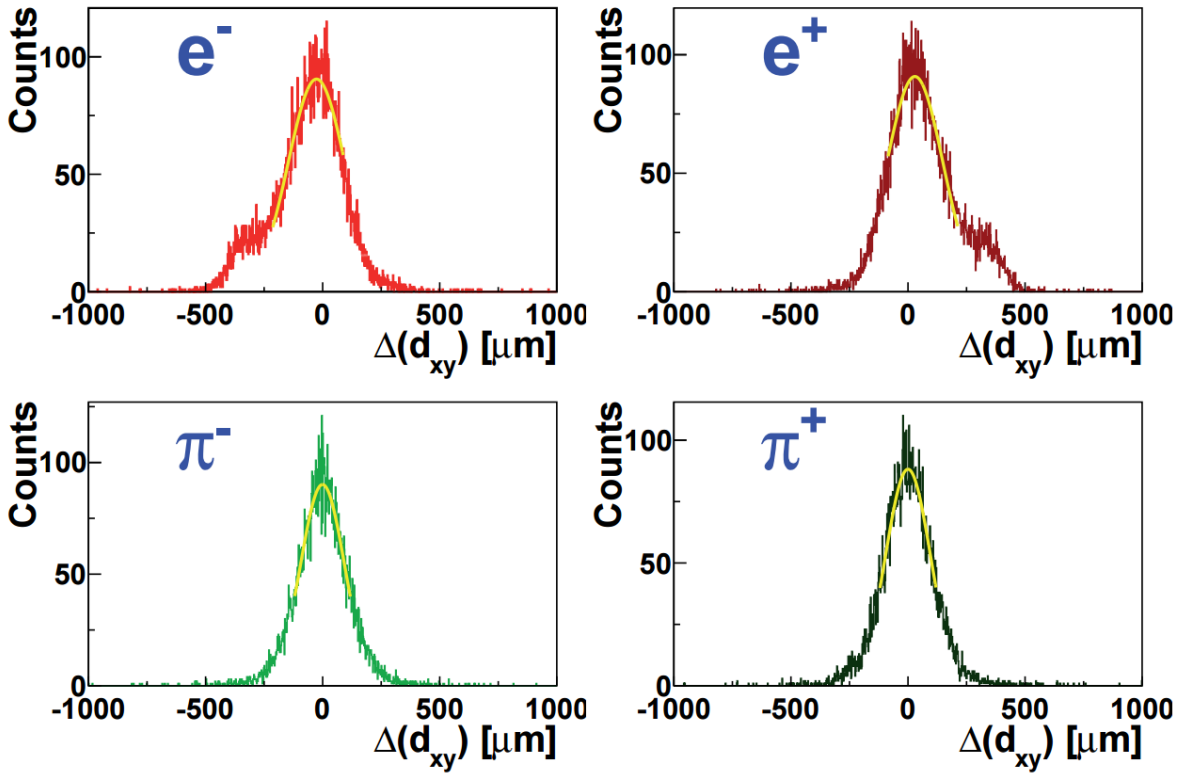

Figure 3.2: Sample Gaussian fit on residuals between measured and expected impact parameter for p_T in the range of 0.5 to 0.6GeV/c [7].

The resolution of electrons and positrons, considering the transverse plane, for low p_T values, is deeply affected by the effects of Bremsstrahlung. This effect is conspicuously shown it the top two graphs for the electron and positron gaussian fits. In these curves, the humps seen to the left of the distribution for electrons, and to the right of the distribution for positrons, are due to the Bremsstrahlung effects.

3.1.7 Time of Flight (TOF)

The time of flight detector, as the name indicates, is designed to identify particles based on the time interval it takes for each type of particle to traverse through the detector. However, for this concept to work, there must be a well defined time of reference, or t_0, when the initial interaction of the particle with the detector occurs. This time can be considered the trigger for the calculation of the time of flight. To obtain t_0, lets consider the lengths of the particle trajectories, time of flights, and momenta, to be x_j, t_j and p_j, respectively, and where the index j stands for the j-th track. Considering the velocities to be discrete value, and that their dependence on the mass of the particle is respected, they can be written as $v_{e^\pm}$, $v_{\pi^\pm}$, $v_{K^\pm}$ and $v_{p,\bar{p}}$. Generalizing the quantity, it can be rewritten as a function of the mass of the specific particle as $v_j(m_j)$. Alternately, the velocities can be associated to β by $v_j(m_j) = c\beta_j(m_j)$. The trigger time will then be a function of the mass of the particle, for each j-th primary track, is will be given by [14, 43]

$$t_{0_j}(m_j) = \frac{x_j}{v_j(m_j)} - t_j = \frac{x_j}{c\beta_j(m_j)} - t_j. \tag{3.5}$$

Assuming that there are N primary tracks, a mass configuration of the type $C(m_1, m_2, ..., m_{j-1}, m_j, m_{j+1}, ...m_{N-1}, m_N)$ can be created, an the weighted average can be calculate over the entire N primary tracks

$$\langle t_0 \rangle (C) = \frac{\sum_{j=1}^{N} \frac{t_{0_j}(m_j)}{\epsilon_j^2(m_j)}}{\sum_{j=1}^{N} \frac{1}{\epsilon_j^2(m_j)}} \tag{3.6}$$

The value ϵ_j stands for the error in t_0, that is, the error of the j-th element of $t_{0_j}(m_j)$, which in turn is dependent on the p_j (or β dependence), x_j, and t_j errors, and is given by

$$\epsilon_j(m_j) = \sqrt{err^2\{\beta_j\}\left(\frac{x_j}{c\beta_j^2(m_j)}\right)^2 + err^2\{x_j\}\left(\frac{1}{c\beta_j(m_j)}\right)^2 + err^2\{t_j\}} \tag{3.7}$$

Next, the value of χ^2 can be calculated through the equation

$$\chi^2(C) = \sum_{j=1}^{N} \left[\frac{t_{0_j}(C) - \langle t_0 \rangle (C)}{\epsilon_j(m_j)}\right]^2 \tag{3.8}$$

for each mass configuration C. Now, the idea it to minimize the value of χ^2 by picking the best mass configuration C_k, for the N primary tracks, with $k = \left\{1, 2, ..., 4^N\right\}$, so that

$$\chi^2_{min.} = \min\left\{\chi^2(C_1), \chi^2(C_2), ..., \chi^2(C_{4^N})\right\} \tag{3.9}$$

assuming that there are 4^N possible configurations, since there are four different types of particles being considered, namely, $e^{\pm}, \pi^{\pm}, K^{\pm}$, and $p/\bar{p}$. The "zero time" t_0 for the event can be computed by finding the mean for the N primary tracks that corresponds to the mass configuration which minimizes χ^2, that is, $\langle t_0 \rangle (C_k)$.

With this information, the probability of an specific track to belong to a certain particle (i.e. $e^{\pm}, \pi^{\pm}, K^{\pm}$, and $p/\bar{p}$), can be derived from the concept of confidence level. If here this confidence is represented by P_C, with $(N-1)$ degrees of freedom, and if the mass configuration of this specific particle is represented by C_y, then this probability of the track belonging to this type of particle is given by

$$w_j(y) = \frac{\sum_{C_y} P_{C_y}(m_y)}{\sum_{C} P_C}. \tag{3.10}$$

It then follows naturally that $w_j(e^{\pm}) + w_j(\pi^{\pm}) + w_j(K^{\pm}) + w_j(p/\bar{p}) = 1$.

Mainly designed for particle identification (PID), the TOF demands high resolution. Having to be able to detect hadrons with momentum in the range of $0.5 GeV/c$ to $2.5 GeV/c$, it must be being able to operate at a time resolution less than $150 ps$. This ensures a reasonably good separation of pions and kaons. But the main focus of this study is to separate electron from these and other particles [44]. Taking a closer look at the resolution of the TOF detector, consider the mass of the particles given by

$$m = p\sqrt{\frac{t^2}{l^2} - 1} \tag{3.11}$$

where p is the momentum, t the time of flight, and l the track length. If the concept of energy is used, it is possible to see that for high momentum values the resolution is predominantly determined by errors in the time and length of travel, than by momentum errors. Equation (3.12) shows that the mass based resolution $\frac{\partial m}{m}$ is comprised of three main terms [44],

$$\frac{\partial m}{m} = \frac{\partial p}{p} \Leftrightarrow \frac{\partial m}{m} = \left(\frac{E}{m}\right)^2 \frac{\partial t}{t} \Leftrightarrow \frac{\partial m}{m} = \left(\frac{E}{m}\right)^2 \frac{\partial l}{l} \tag{3.12}$$

where E is the energy of the particle.

Ultimately, what really matters when using particle detectors it to be able to not only detect an event, but also to identify the type of particle being detected, while being able to distinguish between them by extract useful information about the their particular features. The TOF detector accomplishes this by calculating the time difference (δt) between the instant of time when the traveling particle passes reaches the first counter and the instant of time when it reaches the second counter, as depicted in figure 3.3. Essentially, the concept can be visualized as a chronometer which starts at the moment when the particle enters the first counters, and stops right at the moment exits the second counter.

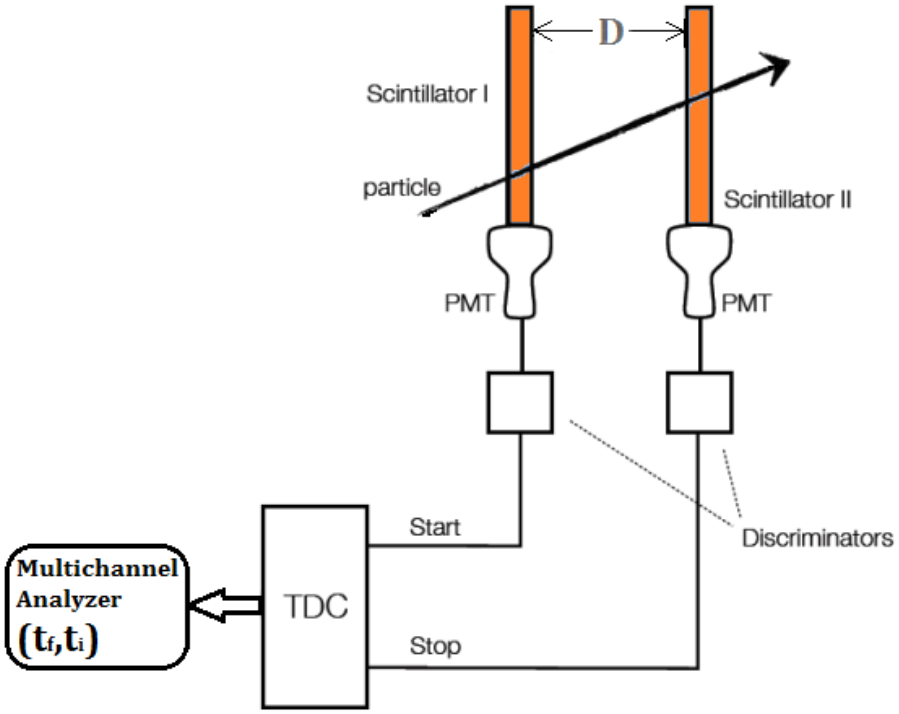

Figure 3.3: Illustration of the time of flight concept: time counting starts when the particle enters the first counter, and stops when the particle exits the second counter [8].

The time difference, i.e. the time of flight, obtained by measuring the time of arrival of the particle at the two different counters, that is, initial time t_i and final time t_f, can be calculated by [8]

$$\delta t = \frac{D_{if}}{v} = \frac{D_{if}}{\beta c} = t_f - t_i \tag{3.13}$$

In order to differentiate between the time of flight of two different particles, for example, the parameters mass, velocity, and energy of the two distinct particles can given by the sets $(m_1, \beta_1 c, E_1)$, corresponding to the parameters of the first particle, and $(m_2, \beta_2 c, E_2)$, corresponding to the parameters of the second particle. Assuming that the value of momentum is

identical for both particles, the time difference in the time of flight can be written as

$$\begin{aligned}\Delta t &= |\delta t_1 - \delta t_2| \\ &= \left| \frac{D_{if}}{\beta_1 c} - \frac{D_{if}}{\beta_2 c} \right| \\ &= \frac{D_{if}}{c} \left| \frac{1}{\beta_1} - \frac{1}{\beta_2} \right| \end{aligned} \tag{3.14}$$

Considering the fact that for relativistic particles the limit value for β is equal to one as the velocity v approaches the value of the speed of light c,

$$\lim_{v \to c} \beta(v) = 1,$$

and that $m_0 c^2 \ll cp \approx E$, equation 3.14 can be rewritten as

$$\begin{aligned}\Delta t &= \frac{D_{if}}{c^2 p} |E_1 - E_2| \\ &= \frac{D_{if}}{c^2 p} \left| \sqrt{(cp)^2 + (m_1 c^2)^2} - \sqrt{(cp)^2 + (m_2 c^2)^2} \right| \end{aligned} \tag{3.15}$$

Because the first squared term inside the square roots are much greater than the second squared term, one can approximate equation 3.15 by

$$\Delta t \approx \frac{D_{if}}{c^2 p} \left| \left(cp + \frac{m_1^2 c^4}{2cp} \right) - \left(cp + \frac{m_2^2 c^4}{2cp} \right) \right| \rightarrow \tag{3.16}$$

$$\Delta t = \frac{c D_{if}}{2p^2} \left| m_1^2 - m_2^2 \right|. \tag{3.17}$$

Using equation 3.17 a comparison between the times of flight of two particles of different mass can be obtained. Taking an electron, for example, which has mass equal to $0.511 \frac{MeV}{c^2}$, a pion, which mass is equal to $139.57 \frac{MeV}{c^2}$, a momentum value of $p = 1.5 \frac{GeV}{c}$ for both particles, and a distance of $D_{if} = 3.5m$ between counters, the difference in times of flight turns out to be $\Delta t \approx 50.54ps$. If the resolution of the detector is $\sigma_t = 100ps$, and the minimum required sensitivity is $\Delta t \geq 4\sigma_t$, then it is straight forward that the separation of electrons and pions is not going to be possible. The separation power, defined as

$$n_{\sigma_t} = \frac{\Delta t}{\sigma_t} \tag{3.18}$$

can be used to check if the minimum difference in time of flight between the two particles is met. In the case of an electron and a pion, at a resolution of $100ps$ for the detector, the separation power turns out to be $n_{\sigma_t} = 0.51$, falling way below the minimum required of $n_{\sigma_t} = 4$.

If a momentum value of $p = 0.5\frac{GeV}{c}$ is considered, the separation power becomes $n_{\sigma_t} = 4.55$, therefore being a momentum region suitable for electron pion separation. The problem is that very few particles in this region were found for the data set used in the analysis, as can be seen in chapter 4. Now, if another pair of two different particles are considered, a pion and a Kaon, with mass equal to $493.68\frac{MeV}{c^2}$, for example, at the original momentum value of $p = 1.5\frac{GeV}{c}$, the difference in time of flight of the two particles, and the separation power, are found to be $\Delta t \approx 581.76ps$ and $n_{\sigma_t} = 5.82$, respectively. In this case the minimum separation power of 4 is surpassed, and the two particles can be distinguished with relative ease. In figure 3.4 it is possible to observe the goodness of separation for different pairs of particles, based on the separation power as a function of momentum. It is straight forward to see that the distinctions between $e^{\pm}$ and $\pi^{\pm}$ only becomes significant for momentum values much lower than $1GeV/c$.

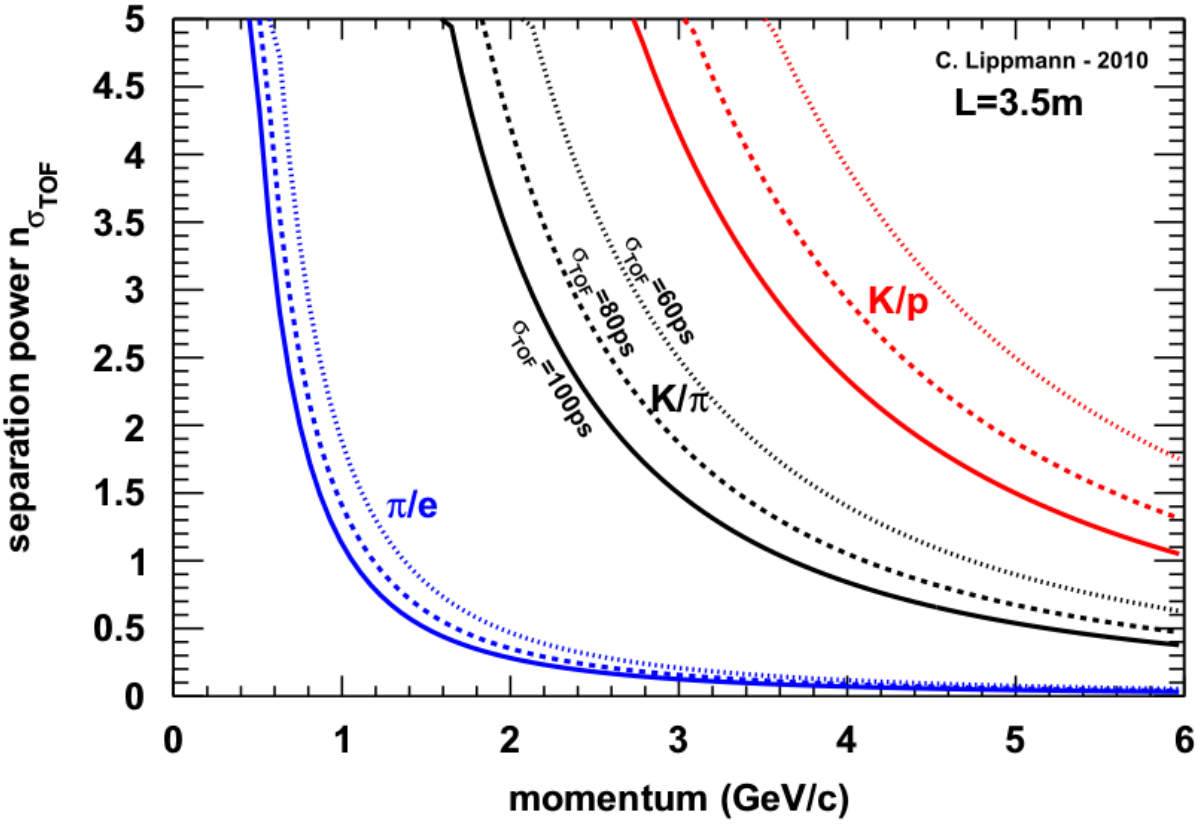

Figure 3.4: Example of a typical TOF array performance at a system time resolution of 60, 80, and 100ps, at $R = 3500mm$ from vertex, with a 90° particle emission [4].

As with any electronic device, there are variations, or jitter, that may affect the time resolution of the apparatus. Table 3.1, taken form the Technical Design Report of the TOF, shows the different possible time related jitters.

Table 3.1: Estimate of time resolution for the ALICE TOF System [14].

Parameter	Average value (ps)	Maximum value (ps)
σ_{T_0}	50	50
σ_{MRPC}	50	80
σ_{TDC}	25	50
σ_{Clock}	15	15
σ_{ClTRM}	10	10
Total	**82**	**120**

In this table, σ_{T_0} is the uncertainty of the trigger time, σ_{MRPC} the Multigap Resistive Plate Chambers, σ_{TDC} the High Performance Time to Digital Converter, σ_{Clock} the clock distribution, and σ_{ClTRM} the error introduced by the distribution of the clock in the Time to Digital Converter to the Readout Modules. The total time jitter can then be given by [14]

$$\sigma_{Total} = \sqrt{\sigma_{T_0}^2 + \sigma_{MRPC}^2 + 2\sigma_{TDC}^2 + 2\sigma_{ClTRM}^2 + \sigma_{Clock}^2} \tag{3.19}$$

Because the main type of particle interaction is the pp collisions, it is expected to find less background contamination generated by heavy ion collision, such as the $Pb-Pb$ collisions. For this reason, it is possible to separate the $e^{\pm}$ from the other particles, therefore making PID of electrons and positrons, viable.

Table 3.2: Estimated efficiency and contamination for a simulated example of pp collision at $\sqrt{s} = 14TeV$. The generated primary particles were in the region $|\theta - 90°| < 45°$ and were tracked by a magnetic field of $\mathbf{B} = 0.2T$ [14].

Primary Particle	Momentum Range (GeV/c)	Efficiency (%)	Contamination (%)
$e^{\pm}$	$0.1 < p < 0.5$	23	8
$\pi^{\pm}$	$0.5 < p < 2.0$	73	8
$K^{\pm}$	$0.5 < p < 2.0$	29	1
p / $\bar{p}$	$0.5 < p < 2.0$	45	0

To illustrate the concept, table 3.2 delineates some statistical values of efficiency and contamination for a simulated example of pp collision with center of mas energy of $\sqrt{s} = 14TeV$. In this example, primary particles were generated in the region $|\theta - 90°| < 45°$ and tracked by a magnetic field of $\mathbf{B} = 0.2T$.

3.1.8 Time Projection Chamber (TPC)

ALICE's TPC main function is to measure energy loss as a function of distance traveled, and to participate in in the momentum measurement for charged particles. In ALICE's central barrel section, the TPC is the main detector responsible for the tracking of the particles, being able to provide particle identification and vertex determination. It detects signals originated from leptons and hadrons for transverse momentum values lower than about $10GeV/c$ and pseudorapidities (η) lower than 0.9. The observables that the TPC aim to detect are hadronic from $Pb-Pb$ collision, but leptonic decays are specifically interesting in the case of heavy flavors. The TPC chamber has a volume capacity of $88m^3$ and is filled with a mixture of drift gases, composed of 90%Ne and 10%CO_2 and operates at a uniform drift field of 400V/cm. The temperature can have a huge effect on the $e^{\pm}$ drift velocity, reaching a variation of 0.34%/degree. For this reason, the temperature is aimed to stay below 0.1°C. A summary of some of the TPC requirements are [45]:

1. Hadronic
    - Over eighty-five percent (85%) track matching to TOF and ITS.
    - At least eight percent (8%) dE/dx resolution.
    - Two-track resolution (at high **B** fields).
2. Leptonic
    - Over ninety percent (90%) for $p_T > 1GeV/c$.
    - Greater than two and a half percent (2.5%) momentum resolution.
    - Better than ten percent (10%) dE/dx resolution for $e^{\pm}$ identification in $Pb-Pb$ high-multiplicity.
    - Central collision rates of up to 200Hz for $e^{\pm}$ inspection and tracking.

Naturally, the accuracy of the readout are of extreme importance, therefore, it is worth the while, just as for the TOF, to take a closer look a the factors that influence the resolution and, ultimately, the results.

The transverse momentum and position resolution are intrinsically affected by the magnetic field and the curvature (S) by the relation

$$\boldsymbol{p}_T = \frac{0.3\mathbf{B}}{S} \tag{3.20}$$

In order to determine the radius $r = S^{-1}$ of a track segment, it is necessary to fit individual space points, giving the resolution $r\delta\phi$ along the trajectory. The azimuthal angle resolution of a single

space point gives a transverse momentum error of

$$\frac{\Delta p_T}{p_T^2} = \frac{40 r\delta\phi}{\mathrm{B}l^2}\sqrt{\frac{5}{n+4}} \tag{3.21}$$

where n is the total number of space points in the particles flight path and l the length of the track. The parameters are determined either by the TPC design, e.g. B and l, or by the design of the readout chambers, e.g. $r\delta\phi$ and n [45, 46]. Equation (3.21) does not take into considers factors such as energy loss and multiple scattering, but rather assumes momentum determination only by the TPC [45, 47].

Besides momentum uncertainties, it is also important to consider the uncertainties in the energy variation. The physical characteristics of the TPC, may impose limitations and certainly exerts influence on the resolution of the dE/dx measurements. The readout chamber has a pad plane composed of 570132 individual pads. The thickness of the material, or the pad length, plays a crucial role in the dE/dx resolution. An empirical model of the dE/dx resolution can be given by [45, 48]

$$\frac{\Delta\frac{dE}{dx}}{\frac{dE}{dx}} \approx \frac{5.745}{(L\cdot N)^{0.37}} \tag{3.22}$$

where L is the pad length and N the number of points per track. However, a different model proposed by Allison and Cobb focused on smaller length pads, yielding better resolution, is corroborated with ALICE's microscopic simulations. This better parametrization defines the dE/dx resolution as [45, 49]

$$\frac{\Delta\frac{dE}{dx}}{\frac{dE}{dx}} \approx \frac{0.409}{L^{0.32}\cdot N^{0.46}} \tag{3.23}$$

The high demands of the TPC for maximum momentum and dE/dx resolution, as well as for correlation studies with two tracks, makes optimization of the detector a challenging feat. An ideal combination of readout granularity and speed to process the data, must be achieved for optimized performance. Also, an ideal combination of drift field voltage and low diffusion gases is sought for acceptable momentum resolution. Because of these reasons, conducting controlled simulations help understand the overall performance of the detector. For instance, electromagnetic interactions in the TPC's gas with the primary particle release primary $e^{\pm}$, which yields a distribution of these $e^{\pm}$ that fit a Poisson type distribution according to the following expression

$$P(x) = \left(\langle x\rangle e^{\frac{x}{\langle x\rangle}}\right)^{-1} \tag{3.24}$$

where x is the distance between two consecutive collisions, and $\langle x\rangle$ the mean distance among

the primary ionizations, which in turn is given by

$$\langle x \rangle = \left[n_p \cdot \Phi \left(\beta\gamma \right) \right]^{-1}. \tag{3.25}$$

The term Φ is the Bethe-Bloch equation that takes the form

$$\Phi \left(\beta\gamma \right) = \frac{K_1}{\beta^{K_4}} \cdot \left[K_2 - \beta^{K_4} - ln\left(K_3 + \frac{1}{\left(\beta\gamma \right)^{K_5}} \right) \right] \tag{3.26}$$

with $K_1, ..., K_5$ being free fitting parameters [47]. The cascade effect producing secondary electrons/positrons, originated from the ionization of high kinetic energy primary electrons/positrons, generates a cluster containing $n_{e^\pm}$ electrons/positrons and can be calculated by

$$n_{e^\pm} = \frac{E_t - I_p}{E_{ei}} + 1 \tag{3.27}$$

where E_t is the total energy dissipated during the collision process, I_p the first ionization potential, and E_{ei} the effective energy needed to generate an electron-ion pair. These clusters are composed of both primary and secondary electrons, without distinctions, and are dimensionally considered to be point like.

There are other factors that influence the performance of the TPC, and one main factor is the diffusion of the $e^\pm$ during drifting. Adopting the defined ALICE's global coordinate system, as shown in figure 3.5, it is possible to describe the $e^\pm$ cloud. The $e^\pm$ conglomerate, or cloud, can be described by the three-dimensional normal distribution

$$P \left(x, y, z, \right) = P_x \cdot P_y \cdot P_z. \tag{3.28}$$

Each individual term, one for each dimension of space, i.e. x, y, and z, is given by

$$P_i = \frac{1}{K_j \sqrt{2\pi L}} e^{-\frac{1}{2L}\left(\frac{i - i_0}{K_j} \right)^2} \tag{3.29}$$

with $i = \{x, y, z\}$ and $j = \{T, L\}$, being T the transverse and L the longitudinal directions. In the case of ALICE, the longitudinal axis is the z axis, and the transverse axis are the x and y axis. The quantities K_j are the diffusion constants, and L the distance that the $e^\pm$ drifted. The coordinates in the second term of the numerator of the exponential, x_0, y_0, z_0, constitutes the point where the event associated with the $e^\pm$ creation took place.

Non-uniformity of the electromagnetic fields inside the drift chamber is also a factor that influences the overall performance of the detector [45]. Because the drift velocity of an $e^\pm$ generated through ionization is directly dependent on the intensity and direction of the electric and magnetic fields, non-homogeneous fields will introduce uncertainties in the measurements.

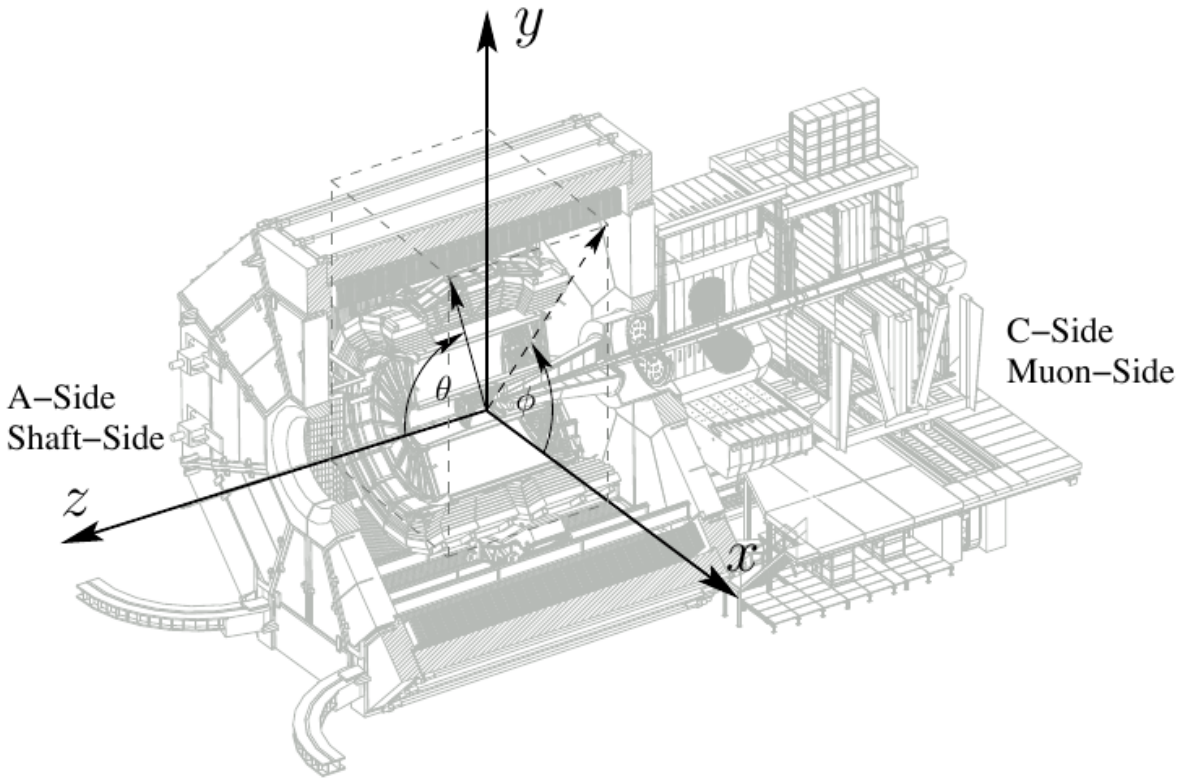

Figure 3.5: ALICE's global coordinate system: ϕ is the azimuthal angle, increasing counter-clockwise, from x to y, i.e. $\phi = 0$ to $\phi = \frac{\pi}{2}$, with the observation reference at positive z; θ is the polar angle and increases form z, or $\theta = 0$, passing by the x-y plane, or $\theta = \frac{\pi}{2}$ all the way to -z, or $\theta = \pi$ [9, 10]

More specifically, if μ is the electron mobility and the quantity $\omega\tau$ is the tangent of the Lorentz angle, the drift velocity of the particles is given by

$$\mathbf{v_{e^{\pm}}} = \frac{\mu}{\omega^2\tau^2 + 1}\left[\mathbf{E} + \omega\tau\frac{\mathbf{E}\times\mathbf{B}}{B} + \omega^2\tau^2\frac{(\mathbf{E}\cdot\mathbf{B})\,\mathbf{B}}{B^2}\right] \tag{3.30}$$

In the case when both fields, **E** and **B** are parallel to each other and uniform overall, the drift velocity is expressed by

$$\mathbf{v}^{\parallel}_{\mathbf{e^{\pm}}} = \mu\times\mathbf{E} \tag{3.31}$$

The positions of the data points in the readout plane, which is composed of pad position and coordinates, the time of detection when reached the front-end electronics, and the magnitude of the signal are all part of the TPC data bundle. The charge clusters generally are not limited to a single time bin neither are concentrated in one single pad, but rather spread over a few of them [9]. For every charge cluster, the center of mass coordinates are given by three points in space, (x, y, z). With a proper knowledge of the drift time, one can obtain the following expression for the center of mass coordinate of the charge cluster

$$\mathbf{r_{cm}} = \mathbf{r_0} + \int_0^{-t_d} \mathbf{v_{e^{\pm}}}\,(x, y, z)\,\mathrm{d}t \tag{3.32}$$

Here $\mathbf{r_0} = (x_0, y_0, z_0)$ represents the charge cluster's center of mass position at the readout plane and $\mathbf{v_{e^{\pm}}}$ the electron/positron drift velocity vector.

3.1.9 Electromagnetic Calorimeter (EMCal)

Jet quenching is enhaced by the unbiased fast trigger EMCal for high energy jets. It also measures the neutral portion of the jet energy, diminishing the bias introduced by jet reconstruction of only charged particles. Minimization of bias reduces uncertainties and improves the efficiency of the measurements performed on the jet modifications. The EMCal is able to measure a large fraction of jet energy, therefore it limits the sensitivity of the track reconstruction specifically to jet structure, thus enabling a thorough analysis of the jet quenching phenomena. Additional advantages brought about by the EMCal are the improvements it introduces in the resolution of energy and in high transverse momentum photon measurement, neutrally charged hadrons, electrons and positrons. These are important features in the identification of heavy flavor jets [50]

As with any equipment, the EMCal has a certain resolution. The detection of energy is

parametrized by

$$\frac{\sigma}{E} = \frac{c_1}{\sqrt{E}} \oplus c_2 \oplus \frac{c_3}{E} \approx \sqrt{\frac{d_{sin.}}{f_s}} \tag{3.33}$$

where E is the energy of the shower. The constants c_1, c_2, and c_3 correspond to the stochastic fluctuations (e.g. energy deposit, energy sampling, light collection, detector design efficiency, etc.), from systematic effects (e.g. such as shower leakage, detector non-uniformity or channel-by-channel calibration errors), and from electronic noise summed over the towers of the cluster used to reconstruct the electromagnetic shower, respectively. For minimum ionizing particles, the variation with sampling frequency depends also on the scintillator thickness in mm ($d_{sin.}$) and the sampling fraction f_s. One of the main functions of the EMCal is to be able to differentiate between $e^{\pm}$ and hadrons for high values of transverse momentum. This is achieved by looking at the quotient of the ratio of momentum to energy. The momentum utilized in the ratio is obtained in the tracking system, whereas the energy is from the shower detected by the EMCal. To isolate the $e^{\pm}$ originated from heavy flavor decays, a method called displaced vertexing must be used [50]. Basically the discrimination methods consists in analyzing the number of charged particles created through the decay of charm mesons to hadrons, which are lighter particles. Bottom quark decays obeys this phenomena, and tend to generate a substantial amount of charged particles. The largest transverse momentum hadrons are correlated in phase space, indicating a common origin displaced vertex. Using an electron and a hadron produced during the decay, it is possible to reconstruct the displaced semileptonic vertex, which is consistent with the lifetime of a B-meson. This is ideal for the differentiation between electrons originated from heavy quark decays from electrons not generated from heavy flavor decays [51]. To accomplish using the displaced vertex algorithm, a single electron with a substantially high transverse momentum value is used as the catalyst, or trigger event. Then the method searches for hadrons of medium transverse momentum values from a common secondary displaced vertex, within the boundaries of a $dR = \sqrt{\delta\phi^2 + \delta\eta^2)} < 0.1$ cone from the initiation point determined by the trigger electron [50]. From a total of six hits in the inner tracking system, there must be at least four hits corresponding to a particular track in order for the resolution of the displaced secondary vertex to be acceptable. When the matching occurs, the bent plane projection (L) is determined by

$$L_{x,y} = r\frac{\boldsymbol{{}_eP_h}}{|{}_eP_h|} = |r|\,cos\theta \tag{3.34}$$

where r is the vector connecting primary and secondary vertexes and ${}_eP_h$ the 3-momentum obtained by the vector sum of the individual electron and hadron momenta. The key to unlocking the good discrimination between different sources of $e^{\pm}$ is to look at the distribution of the pro-

jection. Symmetry around the value zero is an indication of randomly generated backgrounds, whereas as a substantial bias favoring positive values implies real decays.

4 Results

In this section the outcome of the data analysis is delineated, and the corresponding results are described in detail. The ideas presented herein encompasses two sets of data, namely, Monte Carlo simulations, which were used to understand particle behavior and the corresponding effects caused by introducing data cuts. The entire discussion in sections 4.1 to 4.5 is about the data obtained by Monte Carlo simulations, and *not* in real data obtained by beam collision. Only in section 4.6 is real data used to obtain the results. The Monte Carlo simulation data is associated with experimental data generated in 2012 by the proton-proton beam collisions at $\sqrt{s}$=8TeV, and is used as reference in order to separate the different particles based on their identification code. The concepts of yield and efficiency are introduced and their values are thoroughly studied. This type of analysis was actually feasible due to the fact that the contents of the simulation data are exactly known, i.e. the particles are tagged and therefore are identifiable, thus enabling the accurate differentiation between different particle types. The specific data set utilized for this study was taken from the production cycle LHC16c2, a p-p 8TeV Jet-Jet Pythia8 production anchored to LHC12[c-i] pass2, RAW OCDB, ALIROOT-6181. The data subset was taken from directory number twenty (20) and the runs used were 180720, 182692, 185687, 187488, and 189616.

4.1 Data Selection

A main technique, used to get rid of the unwanted background "noise" caused by the detection of other types of particles in the various detectors (i.e. TOF, TPC and EMCal), consists in the application of parametric "cuts". This implies that certain ranges of values for different parameters, such as velocity based and energy loss based, are eliminated from the data set. Several of these cuts were then introduced as part of the analysis. There was no charge based selection used, that is, both positively and negatively charged particles were accepted. Furthermore, three distinct data filters were investigated, one for the velocity of propagation, given in terms of c (β), by the TOF, one for the parameter corresponding to the rate of energy loss as a function

of the length of travel in the TPC (dE/dx), and one for the energy (E) deposited in the EMCal. The ranges of acceptance for the three cuts were:

(1) $0.97 \leqslant \beta \leqslant 1.03$

(2) $80au \leqslant \frac{dE}{dx} \leqslant 100au$

(3) $0.8c \leqslant \frac{E}{p} \leqslant 1.2c$

The application of these three cuts has ultimately as its primary objective the selection of specific ranges that would enable a separation of the electrons and positrons (e^- and e^+) from the remaining particles. To begin with, each individual cut was applied separately to the MC data, so that the effects of each one would be clear. Naturally, every result depend on the value of particle momentum (p). Based on this fact, each of the parameters presented to wit β, dE/dx, and E/p were plotted as a function of momentum, thus enabling the visualization of what happens to each parameter at different momentum values. The efficiency of the cuts was also calculated by taking the ratio of the number of electrons remaining after the application of the cut, to the original number of electrons initially present in the sample before the application of the cut. In addition, the yield of electrons was calculated by taking the ratio of the number of electrons to the total number of particles present in the sample.

4.2 Mass Spectra

As a first approach to find out the types of particles contained within the data samples and to contribute to the understanding of how the cuts generally behave, a look at the mass spectra of the particles seems to be suitable. According to the theoretical method, the mass of the particles can be calculates by using the relativistic relation of energy and momentum, as shown in equation (2.22). Setting the speed of light to the natural unit $c = 1$, the mass squared values would conventionally be given by calculating the difference between the values of energy squared and total momentum squared as,

$$m^2 = E^2 - p^2. \tag{4.1}$$

Nevertheless, assuming the mass of the particles are to remain constant, there would be energy loss as they travel along the detector, gradually depositing their energy content as they move through the different detector layers. Besides rendering the method an ineffective method of differentiating the electrons from the remaining particles, it would also compromise the accuracy of the mass squared distribution. Furthermore, because the energy values attributed to the particles are the values deposited in the EMCal, the calculated mass square values would pro-

duce a substantial portion of "negative" mass particles. Naturally, the observed phenomenon is an artifact of the fact that heavier hadrons typically loose only a fraction of their energy in the EMCal, whereas electrons loose all of its energy [52]. The unaltered momentum values taken from the time projection chamber, and with the lower values of energy registered in the electromagnetic calorimenter clusters, it is possible to explain the observed negative squared mass distribution:

$$E < p \Rightarrow E^2 < p^2 \Rightarrow E^2 - p^2 < 0. \tag{4.2}$$

Additionally, the limiting factor imposed by the EMCal detector resolution makes mass calculation an inappropriate method to distinguish the electrons from the large amount of events originated from heavier particles, such as pions, for example. This is a restriction intrinsically imposed by the very nature of the instrumentation, with no way around it, making an alternative approach to particles identification a must, as described next.

Instead of using the energy-momentum relation method of obtaining the mass squared of the particles, the mass spectra were calculated using a combination of available parameters in the ".root" file. This alternative approach adopted the use of total momentum (a parameter given by the TPC measurement) and the velocity of propagation of the particles, obtained by taking the ratio of the traveled length to the time of flight (a parameter given by the TOF measurement). The specific equation used to calculate the mass is given by

$$m^2 = \frac{p^2}{c^2}\left(\frac{t^2c^2}{L^2} - 1\right) \tag{4.3}$$

where p is the total momentum, c the speed of light, t the time of flight, and L the length of the path traveled by the particle. Figure 4.1 shows the results obtained by employing equation (4.3), with $c = 1$, to calculate the distribution of mass squared.

The main figure is divided into six different plots. Each individual plot depicts only the data pertaining to a definite interval of momentum, starting with the uppermost left-hand graph, corresponding to the range $0 < p \leqslant 1.0GeV/c$, and ending with the bottommost right-hand graph, which corresponds to $5.0 \geq < p \leqslant 6.0GeV/c$. That is, each individual plot is associated with an specific momentum interval of range $1.0GeV$. Also, the graphs in figure 4.1 show a superposition of two different curves, a blue one representing the total mass without any applied cuts, and a red one, representing only the mass of the particles left over after the application of the three cuts described in detail in the previous section.

The results shown in the subplots of figure 4.1, indicate a peculiar problem when trying to distinguish the peak corresponding to the mass of the electrons. Although it is possible to clearly distinguish the peaks corresponding to the mass squared of the different hadrons,

such as the proton $\left(m^2_{p/\bar{p}} \approx 8.8x10^{-1}GeV^2/c^4\right)$, kaon $\left(m^2_{K^{\pm}} \approx 2.4x10^{-1}GeV^2/c^4\right)$, and pion $\left(m^2_{\pi^{\pm}} \approx 1.9x10^{-2}GeV^2/c^4\right)$, for example, it is still not possible to see any significant distinction between pions and electrons. That is, near the region at $\left(0.511MeV/c^2\right)^2$, which corresponds to the region of electron accumulation, regardless of the cuts being introduced or not, one cannot know what is the pion and the electron contribution to the high peak.

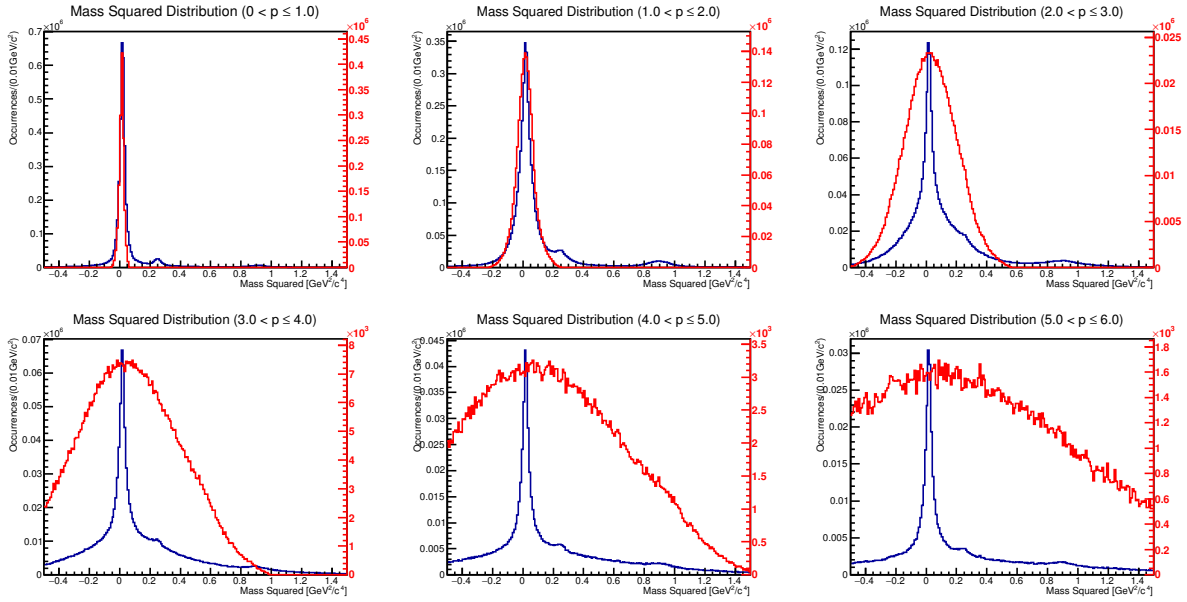

Figure 4.1: Distribution of mass squared calculated using equation 4.3 - Blue Curve → without the application of any cuts; - Red Curve → with the β cut applied.

Figures 4.2 and 4.3 show similar data as figure 4.1, but now with the other two cuts applied, tin other words, figure 4.2 depicts a superposition of the mass squared distribution with itself after the application of the dE/dx cut, and 4.3 with the application of the E/p. In these three sets of plots, for basically all of the momentum ranges, the mass squared distribution yielded a large peak centered at around $0GeV^2/c^4$. Again, this corroborates the fact that the resolution of the detector is not sufficient to separate electrons from pions in the basis of mass calculation, as discussed previously.

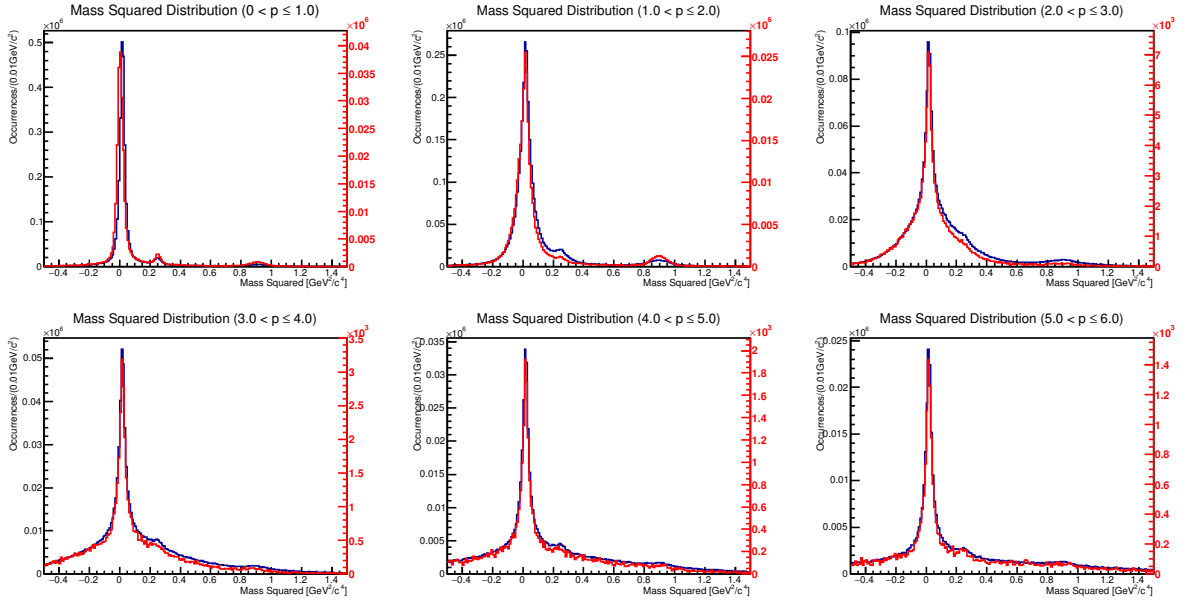

Figure 4.2: Distribution of mass squared calculated using equation 4.3 - Blue Curve → without the application of any cuts; - Red Curve → with the $\frac{dE}{dx}$ cut applied.

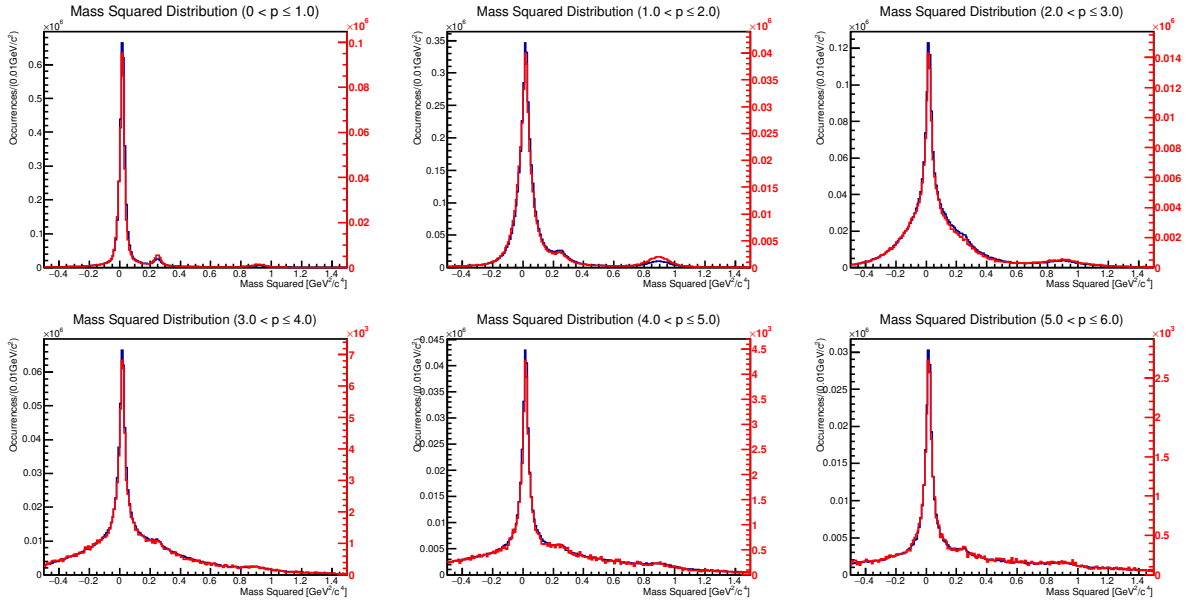

Figure 4.3: Distribution of mass squared calculated using equation 4.3 - Blue Curve → without the application of any cuts; - Red Curve → with the energy over total momentum ($\frac{E}{p}$) cut applied.

4.3 β Cut

The first data selection to be applied individually was the β cut. As a guide for the analysis, and to serve as a beacon for particle identification, a model for an elucidative plot is shown in figure 4.4. This plot shows the parameter beta versus momentum, extracted from a lead-lead ion collision experiment at $\sqrt{s_{NN}}$=2.76TeV. In this graph the different particles are identified

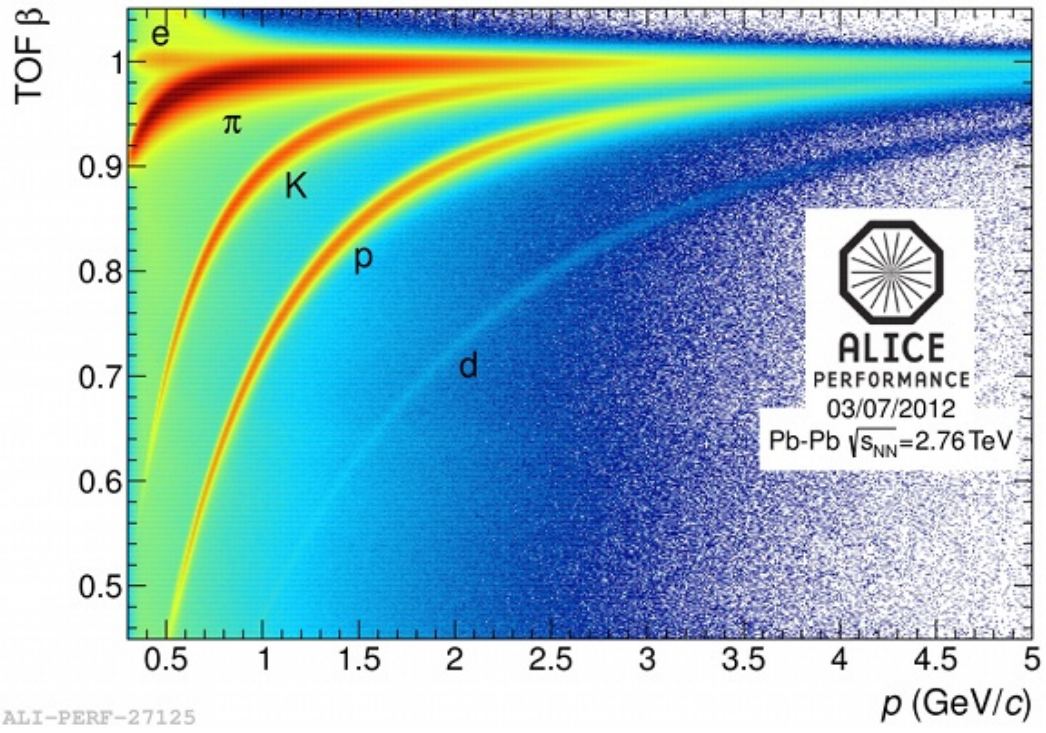

Figure 4.4: Sample graph showing β versus p, for momenta up to 5GeV/c [11]. Different velocity patterns can be observed for each individual particle, specially for lower momentum values.

with the letter corresponding to the official symbol. Each different particle form a different pattern based on the velocity of travel within the TOF detector, which can be readily observed at the lower momentum range. The unique set of characteristics present in this plot can be used as a guide to differentiate between the various particles generated by the collision in real data or by MC simulation. Note that in figure 4.4, the $e^{\pm}$, which are the most important particles for the purpose of this analysis, are virtually indistinguishable from the pions (π^- and π^+) for momentum values greater than about 800MeV/c, because both types of particles merge at the $\beta = 1$ horizontal line. At this point pions are moving with speeds very close to the speed of light. For momentum values greater than approximately 2.5GeV/c, kaons (K^- and K^+) also merge with pions and electrons at the $\beta = 1$ line. For higher values of momenta, protons and anti-protons (p and $\bar{p}$) also start merging with the previously mentioned particles, and so on for the deuterons and other particles that might exist in the sample.

The same type of plot was then graphed for the Monte Carlo simulation data at $\sqrt{s} = 8TeV$, in order to confirm if similar patterns are observable. The corresponding results are shown in figure 4.5. The plot of figure 4.5 was obtained without the application of any cuts, whereas in figure 4.6 a depiction of the same plot can be seen after the application of the cut in beta.

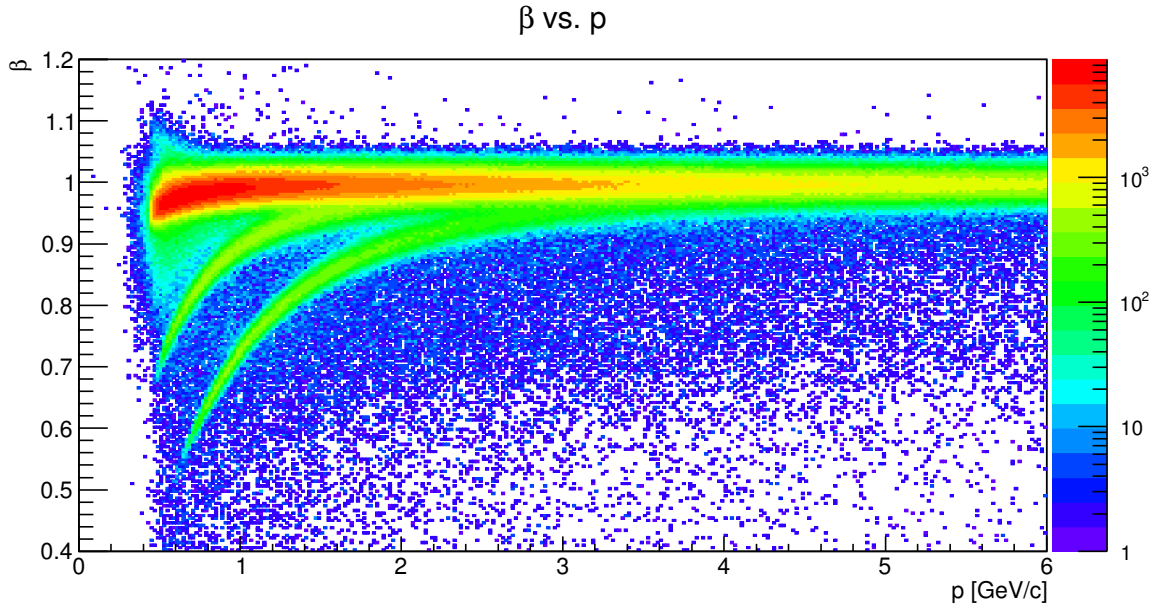

Figure 4.5: Plot of beta (β) as a function of total momentum (p), without any cuts applied for the full range of momentum (0 GeV/c to 6 GeV/c). When comparing with figure 4.4, pions, kaons and protons/anti-protons are clearly seen.

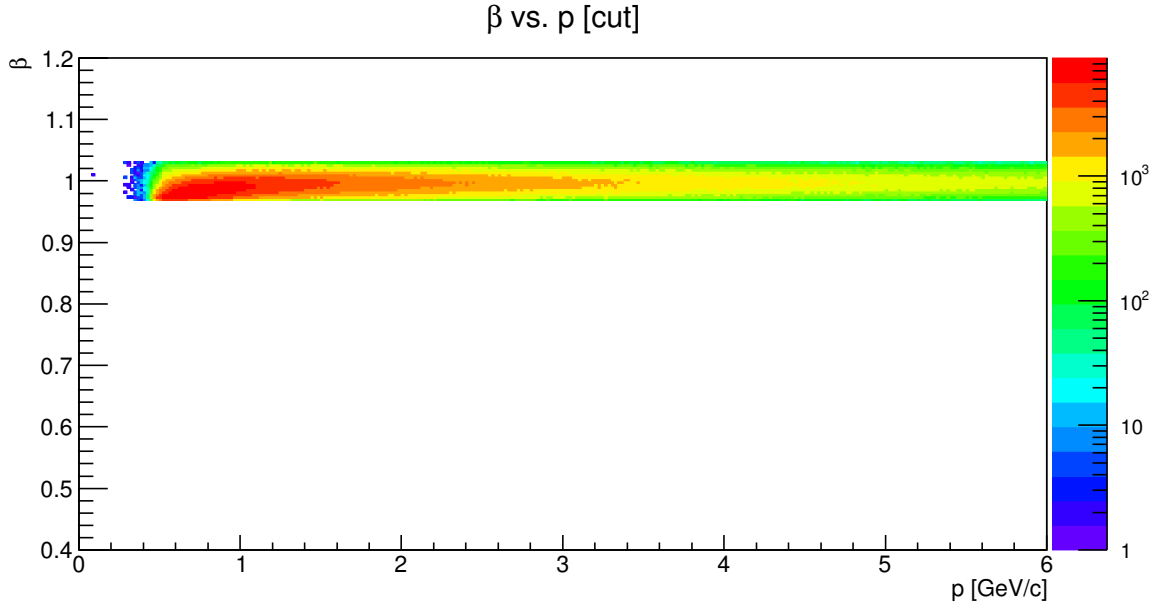

Figure 4.6: Same as figure 4.5, but with cuts applied, i.e. $0.97 \leqslant \beta \leqslant 1.03$.

A brief comparison between these two plots shows that the curved sections corresponding to the heavier particles, namely kaons and proton/anti-protons, at the lower momentum range, can easily be distinguished and therefore eliminated. By just looking at these graphs, it is not trivial what exactly is going on in terms of the electrons, which, after all, is the particle of interest. To compensate for that, an examination of the effects that the cut in β had on the original data had to be done by analyzing two quantities of interested, namely the yield and the efficiency.

The yield is a means to obtain the ratio of the number of electrons to the number of the total particles in the sample. This calculable quantity gives a clear view of how many electrons there are in the sample, and allows a comparison to the total number of the remaining particles in the same sample. The yield was calculated and is given by

$$Y = \frac{N_e}{N_T} \qquad \text{and} \qquad Y^c = \frac{N_e^c}{N_T^c}, \tag{4.4}$$

where N_e and N_T stand for the number of electrons and the total number of particles, before the application of the cut, respectively. The superscript c stands for "cut", so that N_e^c and N_T^c are the total number of electrons and the total number of particles, after the application of the cut, respectively. The total number of each particle can be retrieved from the data files by using particle ID. The graphs depicted in figure 4.7 show the results obtained for the yield calculation, both before (left) and after (right) the application of the beta cut, for different values of momenta. More specifically, the calculation was performed for six different bins of momentum, each spanning $1GeV/c$, that is, six bins of width $1GeV/c$, ranging from 0 to $6GeV/c$. One does not need to look carefully to notice that the proportion of electrons to the remaining particle, does not change considerably after the application of the beta cut. In both cases, before and after the cut, the number of electrons, regardless of momentum value, stayed below 10%.

Another quantity of interest is the efficiency of the applied cut. The efficiency is a measure of how well the specific cut functioned on the data set. It is essentially a technique used to quantify the proportion of the wanted particles that remained in the data sample after the introduction of the cut. It can also be thought as a form to count how many "good" particles were eliminated from the sample, together with the other types of particles that were actually supposed to have been eliminated. For example, if electrons and positrons are the particles of interest, and if the specific cut is efficient, after its application on the data set most of the electrons and positrons will still be present in the sample. That is, very few electrons and positrons will be lost in the process.When the remaining number of electrons and positrons is compared to the original number before the application of the cut, no major loss will be observed. The

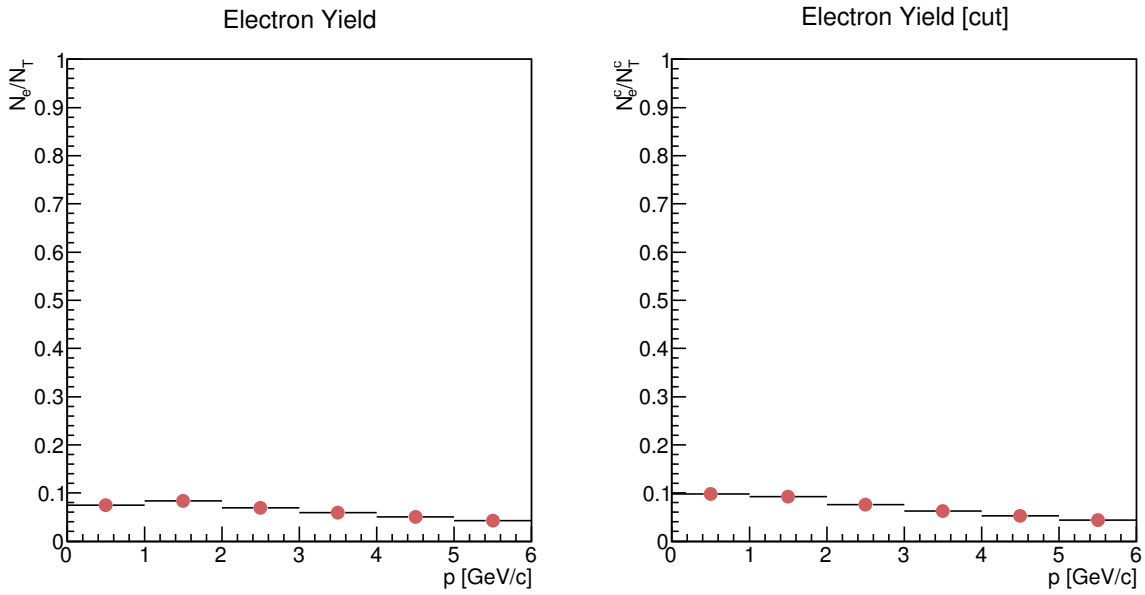

Figure 4.7: Yield of e^- and e^+ calculated by taking the ratio of the number of e^- and e^+ to the total number of particles present in the sample. The plot on the left depicts the yield before the application of the β cut, whereas the plot on the right shows the yield after the cut.

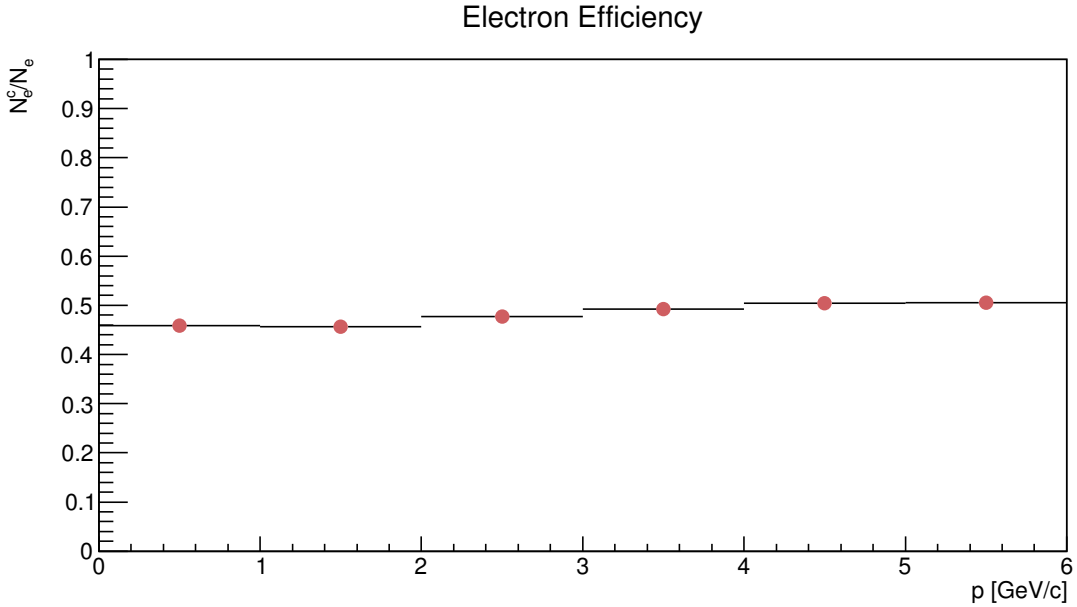

Figure 4.8: Efficiency of the e^- and e^+ calculated by taking the ratio of the number of e^- and e^+ remaining after the application of the β cut, to the original number of e^- and e^+ initially present in the sample before the application of the cut.

calculation of the efficiency is done by taking the ratio of the remaining electrons post-cut, to the number of electrons pre-cut, and is given by

$$\epsilon = \frac{N_e^c}{N_e} \tag{4.5}$$

where N_e^c is the number of electrons and positrons left after the cut, and N_e the number of electrons and positrons originally present in the data sample.

Using the same number of bins, of same width ($1GeV/c$) used in the calculation of the yield, the plot of efficiency is shown in figure 4.8. It is possible to observe that the efficiency of the beta cut for electrons is quite poor. By simply eliminating beta values below 0.97 and above 1.03, the number of electrons drop drastically to less than 50% of the original number.

Given these results, it it straight forward to conclude that a cut in beta does not aid in the separation of electrons from the remaining particles. On the contrary, using a beta cut eliminates a lot of electrons from the sample.

4.4 dE/dx Cut

One of the most common methods of differentiating between particles is to look at the rate of particle energy loss as they travel along the detector layers. More specifically, the ratio of the lost energy to distance traveled is registered as a parameter of the time projection chamber, or the TPC signal given in arbitrary units.

By analyzing equation 2.39, one observes that the $1/v^2$ factor from the β^{-2} term outside the square bracket, varies at a faster rate with varying velocity than does the $ln(v^2)$ term within the square braket. This implies that the rate of energy loss initially decreases as energy, or momentum, increases. As the velocity approaches relativistic values, the rate of energy loss starts to increase as energy and momentum increases. This behavior suggests that a variation in the TPC signal filters may actually improve electron efficiency.

Figure 4.9 depicts a sample plot showing the TPC signal, as a function of momentum, for a proton-proton beam collision at $\sqrt{s}$ =7TeV. In this plot the distinct patterns, generated by the distinct types of particles, are clearly noticeable. Take, for example, the energy loss of the $e^{\pm}$. It is possible to observe an accumulation of electron/positron tracks at around a TPC signal value of approximately 70a.u. At $p \approx$0.55GeV/c and $p \approx$1.1GeV/c, the intersection of kaons and protons/anti-protons, respectively, is observed. For these specific values, the contamination of these particles in the electron distribution is significant and, using solely energy loss as a means to separate them, proves to be inefficient. Just as with the β cut, the cut in dE/dx was applied to the same MC data used previously. Figure 4.10 shows the results obtained. It is possible to see a conspicuous accumulation of $e^{\pm}$ located in a band lying between the TPC signal values of $\approx$ 80 and 100 a.u. In this band, at approximately $p \approx$0.6GeV/c and $p \approx$1GeV/c, it is possible to observe yellowish areas where there is a high concentration of kaons and protons/anti-protons,

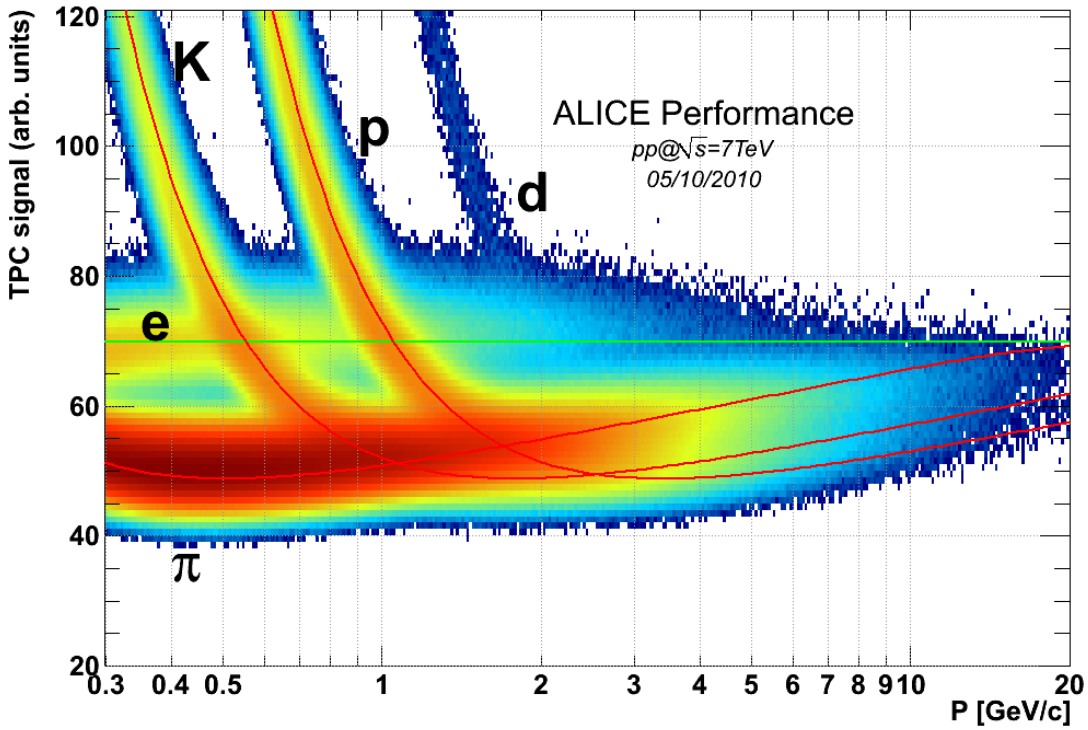

Figure 4.9: Sample graph showing $\frac{dE}{dx}$ versus p, for momenta up to 20GeV/c [12]. Different rates of energy loss can be observed for each individual particle, specially for lower momentum values.

respectively, superimposed upon the $e^{\pm}$, ergo confirming the observation made in figure 4.9.

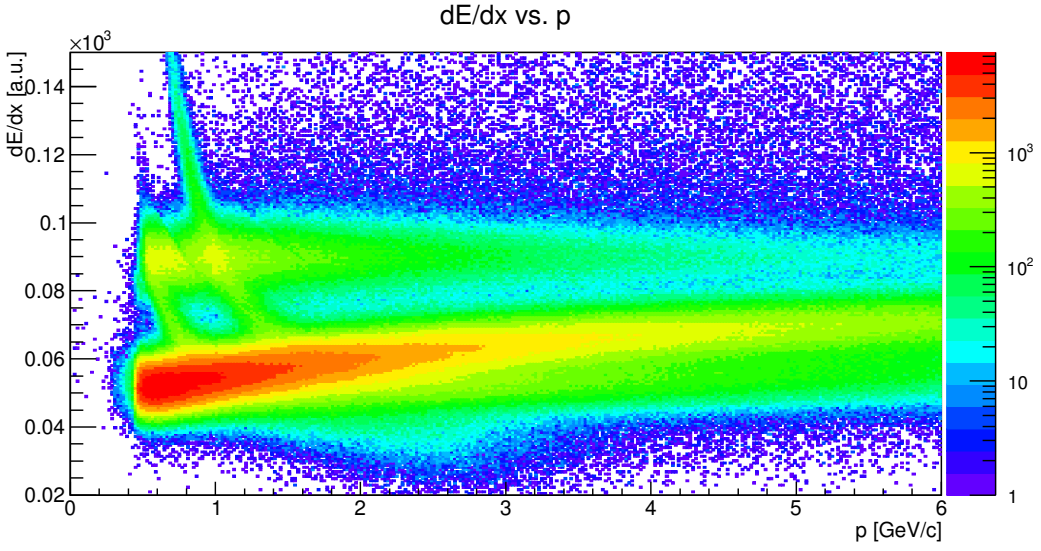

Figure 4.10: Plot of energy loss per distance traveled ($\frac{dE}{dx}$) as a function of total momentum (p), without any cuts applied for the full range of momentum (0 GeV/c to 6 GeV/c). When comparing with figure 4.9, not only pions, kaons and protons/anti-protons are clearly distinguishable, but also e^- and e^+ are conspicuous in the plot.

After the application of the dE/dx cut, that is, accepting tracks between and including 80a.u. and 100a.u., and eliminating anything below 80a.u. and above 100a.u., the plot shown in figure 4.11 is obtained. The plot by itself does not elucidate much by itself, nor the true effects

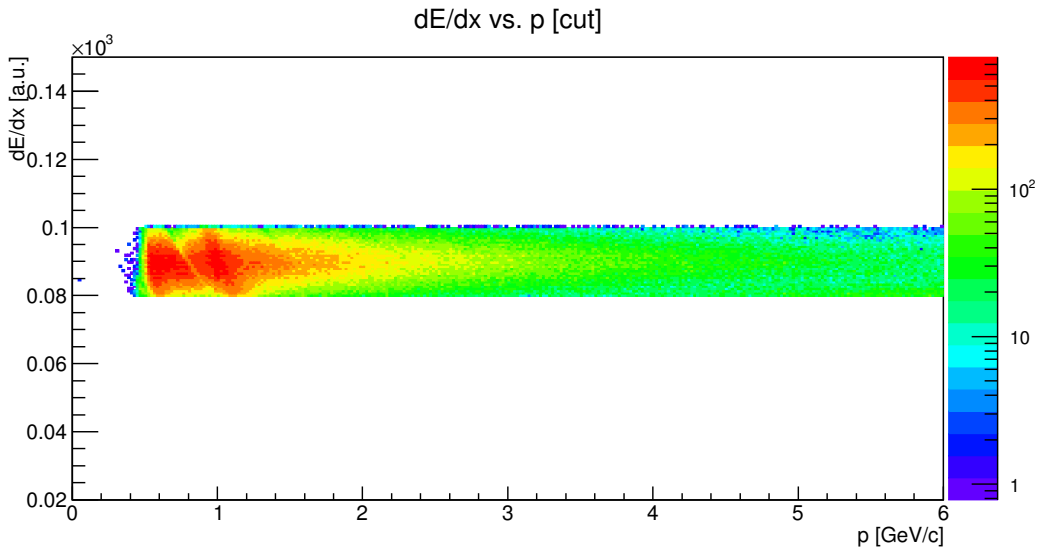

Figure 4.11: Same as figure 4.10, but with cuts applied, i.e. $80a.u. \leqslant \frac{dE}{dx} \leqslant 100a.u.$

of the cut. Nevertheless, the application of the cut allows for the calculation of the yield and the efficiency. These parameters are shown in plots of figures 4.12 and 4.13. Right away, the yield plots show a considerable improvement in the segregation of $e^{\pm}$ from the remaining particles. From an yield average of less than 10% for all six momentum segments, the improvement reaches a mean yield value around or grater than 90% for momentum values ranging from 0 to 4 GeV/c, a mean of almost 90% for momentum values ranging from 4 to 5 GeV/c, and an average of around 70% for momentum values between 5 and 6 GeV/c, as seen in figure 4.12.

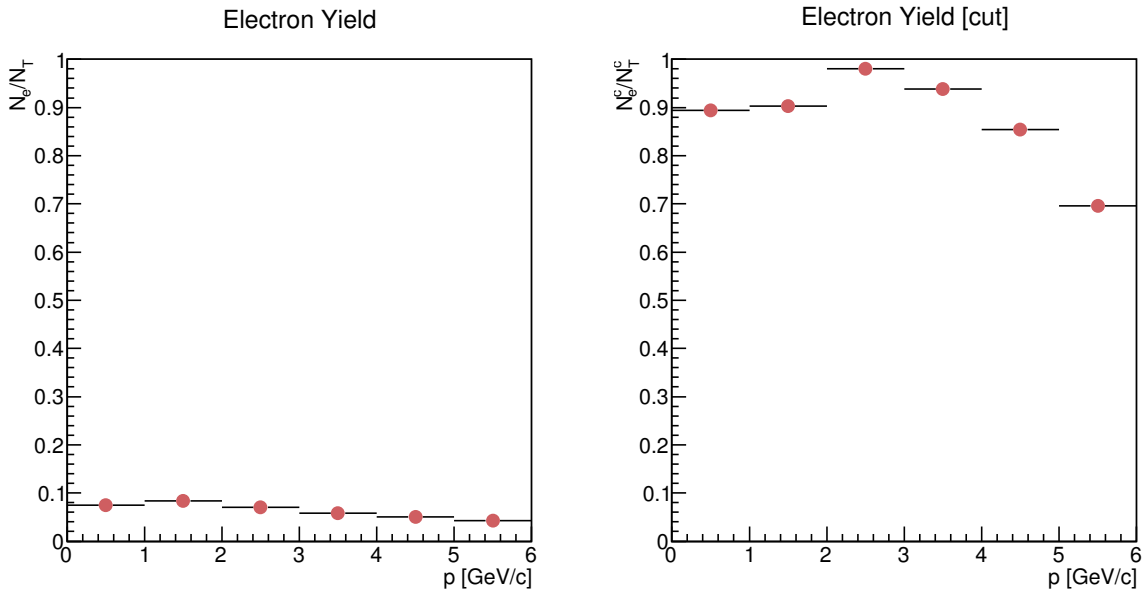

Figure 4.12: Yield of e^- and e^+ calculated by taking the ratio of the number of e^- and e^+ to the total number of particles present in the sample. The plot on the left depicts the yield before the application of the $\frac{dE}{dx}$ cut, whereas the plot on the right shows the yield after the cut.

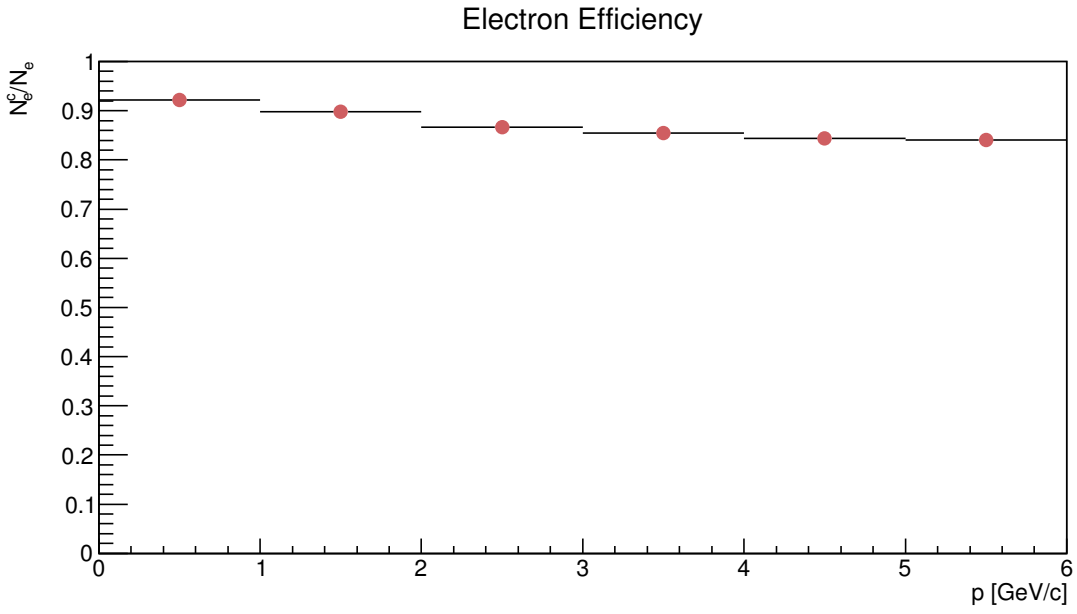

Figure 4.13: Efficiency of the e^- and e^+ calculated by taking the ratio of the number of e^- and e^+ remaining after the application of the $\frac{dE}{dx}$ cut, to the original number of e^- and e^+ initially present in the sample before the application of the cut.

Also, after the application of the dE/dx cut, the electron/positron efficiency obtained was over 84% for all six momentum ranges, as can be seen in figure 4.13. That is, the cut based on

the TPC signal proved to be extremely efficient not only in separating the $e^{\pm}$ from the remaining particles, but also in preserving the majority of the $e^{\pm}$ that were there to begin with.

4.5 Energy to momentum ratio

One of the most common strategies used to distinguish the $e^{\pm}$ picked-up by the electromagnetic calorimeter is to look at the energy to momentum ratio (E/p). In order to take a look at E/p, only the events detected by the electromagnetic calorimeter were considered. This is achieved by matching the reconstructed TPC tracks to the EMCal clusters. This matching is accomplished by extrapolating a reconstructed track to the calorimeter, and then checking the separation between the positions of the track and the clusters. If the distance of separation falls below a certain value, then it is considered a match, otherwise it is discarded. Iteratively, a second pass is done and only the nearest track-cluster pair is selected as the actual match [53], that is, the distance of the track-cluster pair is minimized by comparing the values of the different $\Delta\eta$ and $\Delta\phi$ as they approach zero.

Because of the small mass of $e^{\pm}$, these particles deposit all their energy in the EMCal through $e^{\pm}$ shower, yielding values for the ratio of energy to momentum essentially distributed around "one", i.e. $E/p \simeq 1$ [13]. That is, the sum of the momenta given by the curvature of the track in the high magnetic field of the TPC must be equal (or extremely close) to the total energy deposited in the EMCal. The most common method to perform this analysis is to plot the E/p distribution and check if there's indeed a significant accumulation of events around the value 1, as shown in the graph of figure 4.14. This graph, which exemplifies the concept, was taken from a $\sqrt{s}$=7GeV pp collision for p_T values that fall in the 4 to 5 GeV/c range. In this case, the dashed blue line represents a Gaussian fit of the electrons, whereas the dotted red line represents an exponentially decaying fit for the background particles. The summation of the two yields the solid black line, which represents the actual fit for the entire data set. The pink arrows indicate the lower and upper limits of the integrated area corresponding to the electron distribution. The width of the fit considered in the analysis spans a total of six (6) sigma, that is, -3σ to 3σ, where σ is the standard deviation of the mean (μ).

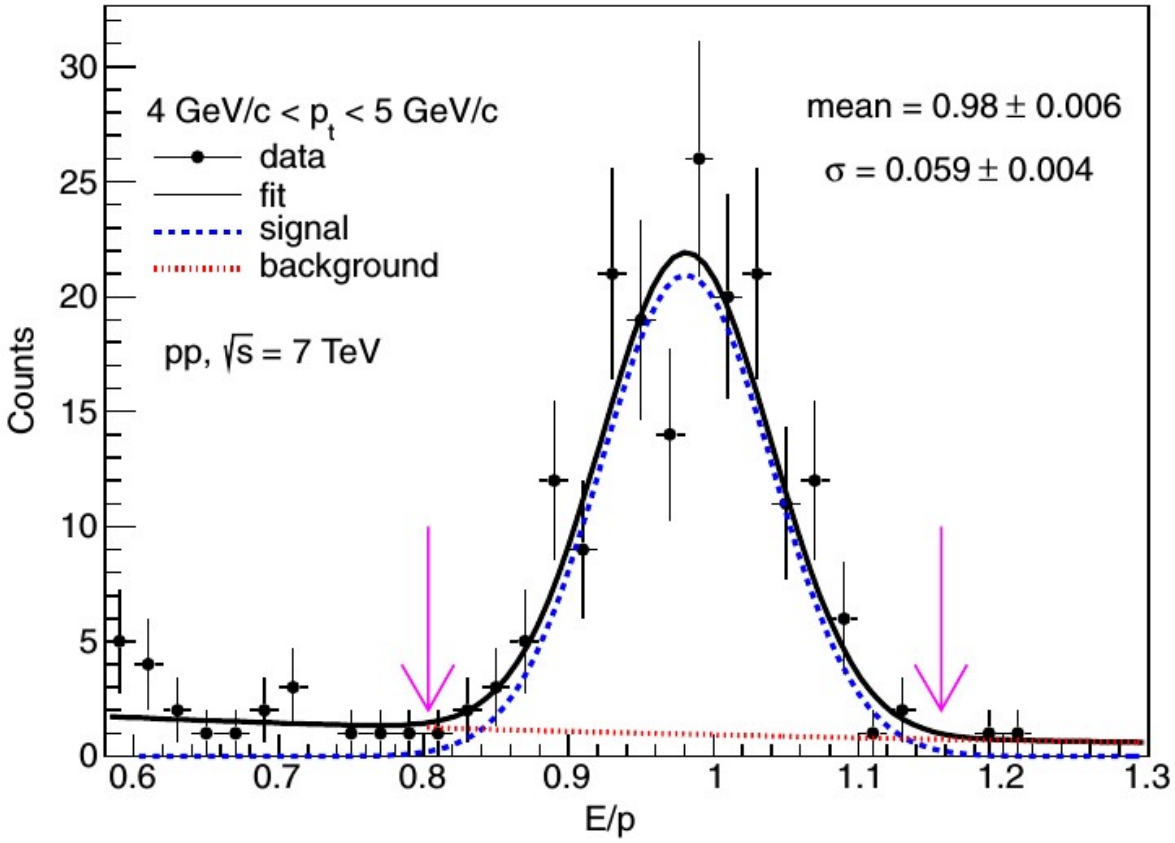

Figure 4.14: Graph showing the E/p distribution, for p_T ranging from 4 to 5GeV/c, of a pp collision at $\sqrt{s}$=7TeV. The total particle distribution (solid black) was fitted by adding the electron distribution fit through a Gaussian function (dashed blue) and the background fit with a decaying exponential function (dotted red). The pink arrows indicate the upper and lower limits of the region used in the analysis [13].

In an attempt to reproduce a similar result using the MC data discussed thus far, several graphs of energy over momentum were obtained. These graphs are shown in figure 4.15 and depict the distribution of events as a function of the E/p values for the same six momentum bands that have been analyzed up to now. Figure 4.16 shows exactly the same information as figure 4.15, except that now it depicts E/p after the application of the second cut, i.e. acceptance of $80au \leqslant \frac{dE}{dx} \leqslant 100au$ only.

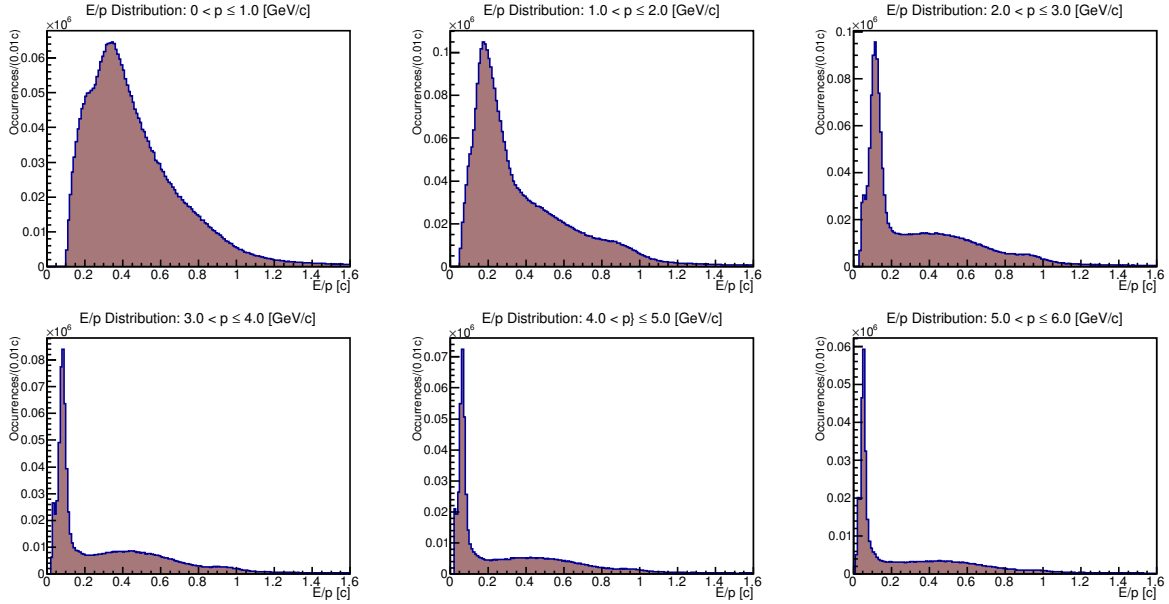

Figure 4.15: Graphs of energy to momentum ratio $\left(\frac{E}{p}\right)$, obtained from the analyzed MC data. These graphs depict the original data and do not include the results of the application of any cuts.

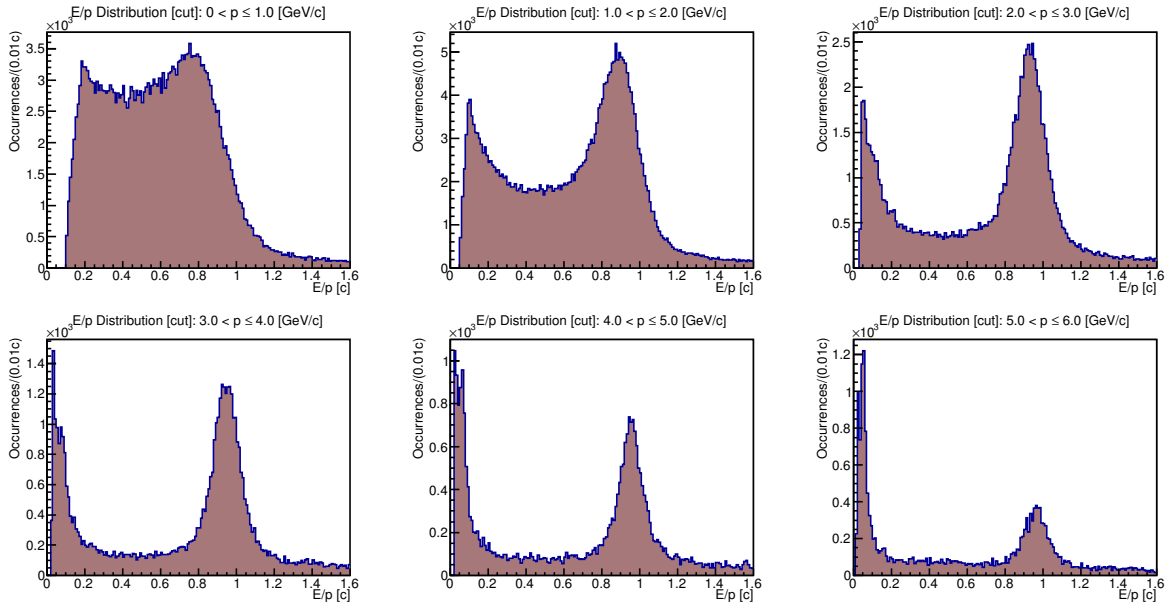

Figure 4.16: Same as figure 4.15, but now showing the results of the $\frac{dE}{dx}$ cut.

Note that the distribution of the values of E/p near the value of 1 is quite evident in the plots of figure 4.16, definitely indicating the presence of $e^{\pm}$ in the analyzed data samples. These plots do not contemplate the differentiation between the electrons originated from the decay of heavy flavor quarks from the ones generated by γ decay into an electron-positron pair ($e^{-}e^{+} \rightarrow \gamma$), or any other channel for that matter. In order to implement an analytical method to eliminate the influence of the electron/positron pair, the concept of invariant mass would have to be taken into account. With these results at hand, it is now possible to observe two peaks, namely the one

distributed around $E/p \simeq 1$ and another just to the left of $E/p \simeq 0.1$. Naturally, there are several other cuts that one can apply in order to better select $e^{\pm}$. However, sticking to the original idea and looking at the graph of figure 4.16, the third type of cut, which seems to be quite straight forward to introduce, is actually the last cut originally mentioned, that is, to accept values of E/p that lie between, and including, $0.8c$ to $1.2c$. To confirm the effects that a cut in E/p has on the data, the analysis was redone, but without consecutively applying the E/p cut to the dE/dx cut seen previously. The results obtained are shown in figure 4.17. Note that in these plots the separation of $e^{\pm}$ from the other particles becomes better as p increases, at least for the six ranges under consideration. This fact can readily be observed by noticing the sharp, flat cut, in the lower limit side of the distributions.

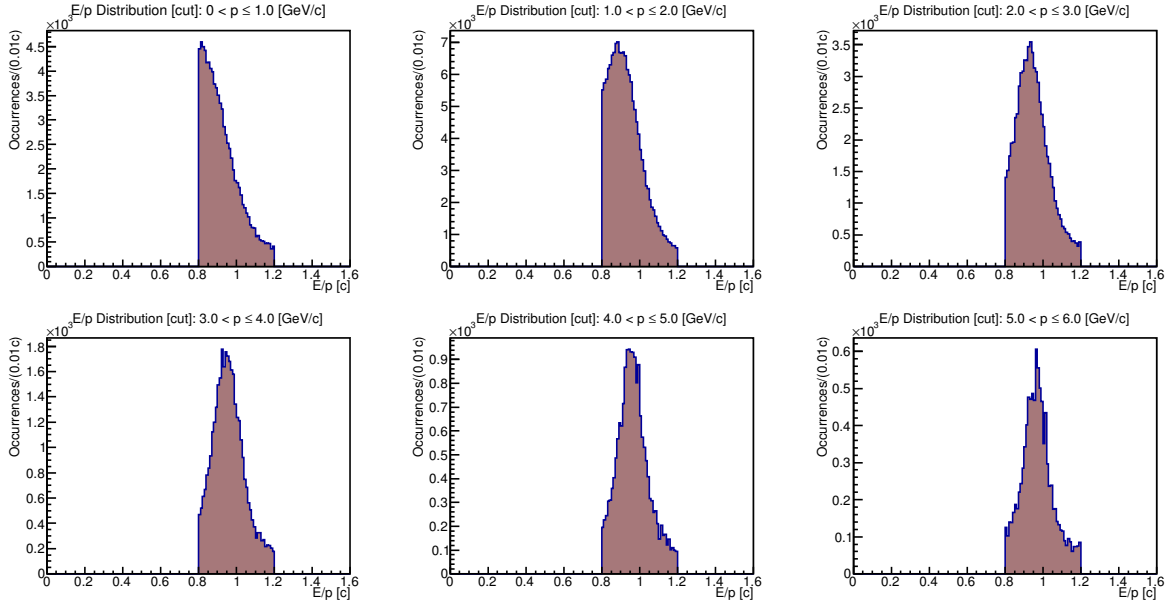

Figure 4.17: These plots are the same as the ones shown in figure 4.16, but now only a portion of the $\frac{E}{p}$ values are shown after the third cut was applied (i.e. $0.8c \leqslant \frac{E}{p} \leqslant 1.2c$).

As with the other cuts, the parameters that interestingly elucidates what is going on are the yield and the efficiency. The plots shown in figures 4.18 and 4.19 depict these two values for the six momentum ranges, respectively. Note that after the application of both cuts, the yield of electrons dramatically increase, nearly reaching the 100% (falling just short of 1) mark for particle momenta between 2 and 3 GeV/c. Nonetheless, the values of efficiency shown in figure 4.19 are very low. Based on this observation, it is important to note again that the $e^{\pm}$ produced from the semi-leptonic decay of heavy flavor quarks are not being distinguished from the other possible sources of $e^{\pm}$. Table 4.1 lists a few reaction channels that yield electrons that may interfere with the identification of heavy flavor decay electrons. Given all these mechanisms for which electrons can be generated, the total number of $e^{\pm}$ left after the application of the cuts would certainly be affected. It is no trivial task separating the electrons generated by heavy

flavor decay from the other electrons generated by a diversity of other processes.

Based on theory and the fact that e^- and e^+ deposit all, or nearly all, of their energy in the EMCal, it is more realistic to consider only those $e^\pm$ that are in the E/p predefined range to begin with. By doing so, the large quantities of particles detected for lower values of E/p do not enter the calculation of yield and efficiency. In other words, the first cut to be applied should be in E/p, and not dE/dx, which should come second. By doing this, one ensures that only the $e^\pm$ that deposit all their energy in the EMCal are considered for the statistics. The results obtained are shown in figures 4.20 and 4.21 for the yield and efficiency, respectively.

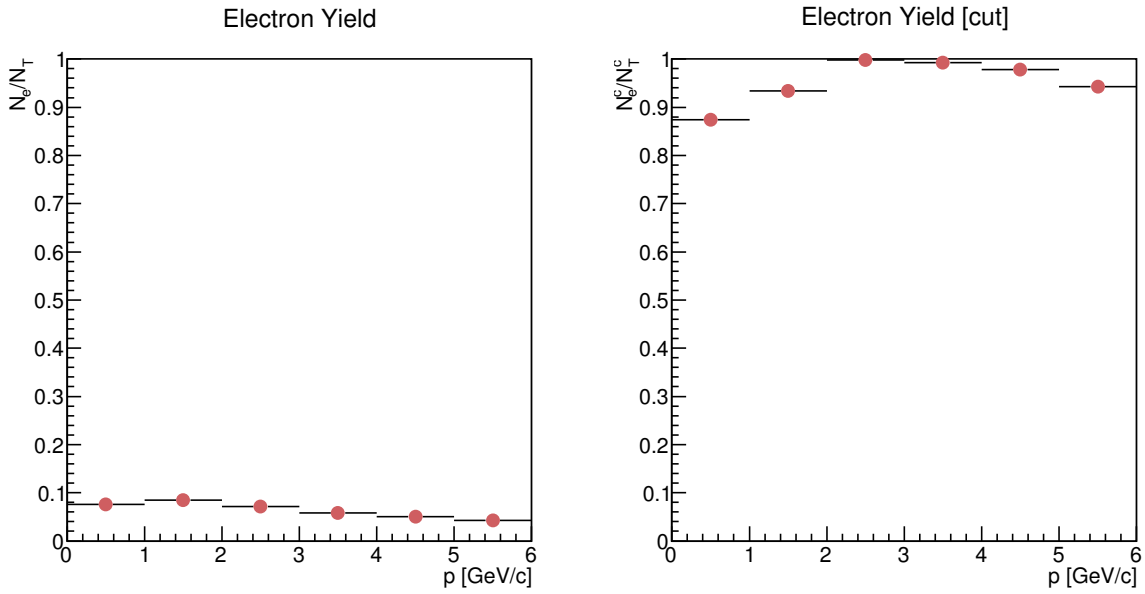

Figure 4.18: Yield of e^- and e^+. The plot on the left depicts the yield before the application of the $\frac{dE}{dx}$ and the $\frac{E}{p}$ cuts, whereas the plot on the right shows the yield after the cuts.

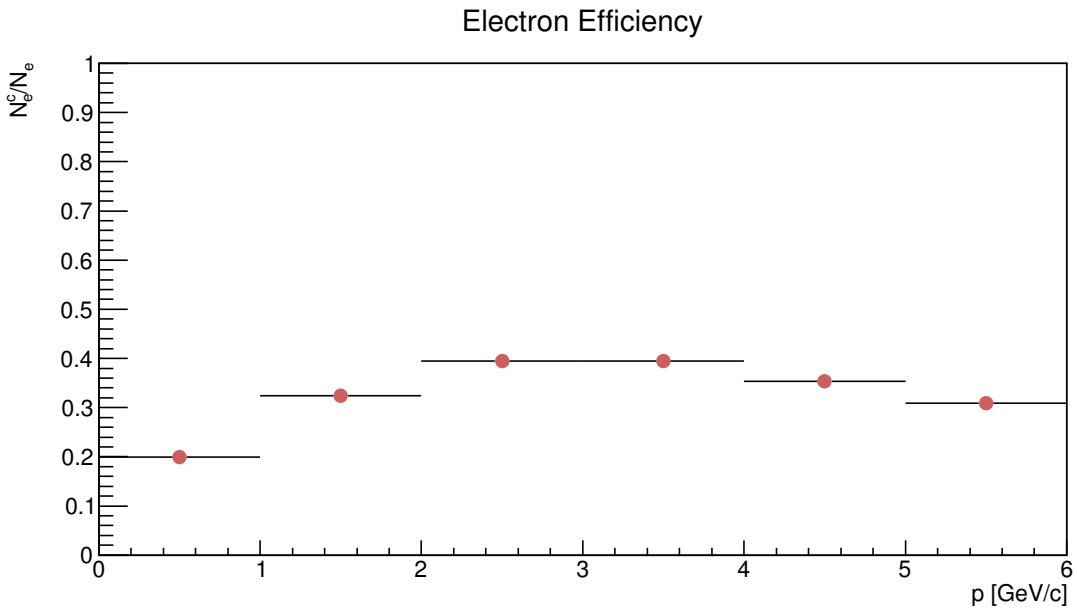

Figure 4.19: Efficiency of the e^- and e^+ after the application of the $\frac{dE}{dx}$ and the $\frac{E}{p}$ cuts, for every $e^\pm$ present in the sample.

Table 4.1: Examples of decay processes that produce electrons and positrons [13, 15, 16, 17].

Type	Process	Description
Photonic	Dalitz	Light meson decay where a neutral pion decays to a photon, electron, and positron trio ($\pi^0 \rightarrow \gamma e^- e^+$).
Photonic	Pair production	The interaction of a photon (real or virtual) with matter produces an electron and positron pair. ($\gamma \rightarrow e^- e^+$)
Nonphotonic	Heavy Flavor	The ρ, ω, and ϕ meson decay is responsible for a smaller quantity of e^- and e^+ production.
Nonphotonic	Quarkonia	Quark decays that take place via the transformation $J/\psi \rightarrow e^- e^+$ are significant in number at the mid range of p_T
Nonphotonic	Misreconstructions	These are due to the K_{e3} misreconstruction of $e^\pm$ tracks, and are significant, about 10%, for lower p_T values (< 1GeV/c) and insignificant for higher p_T values.
Nonphotonic	Drell-Yan	The background contribution is negligible. It occurs when a quark of a hadron and an antiquark of another hadron annihilate, generating a virtual photon that consecutively decays into a pair of leptons of opposite charge, such as an electron and a positron.

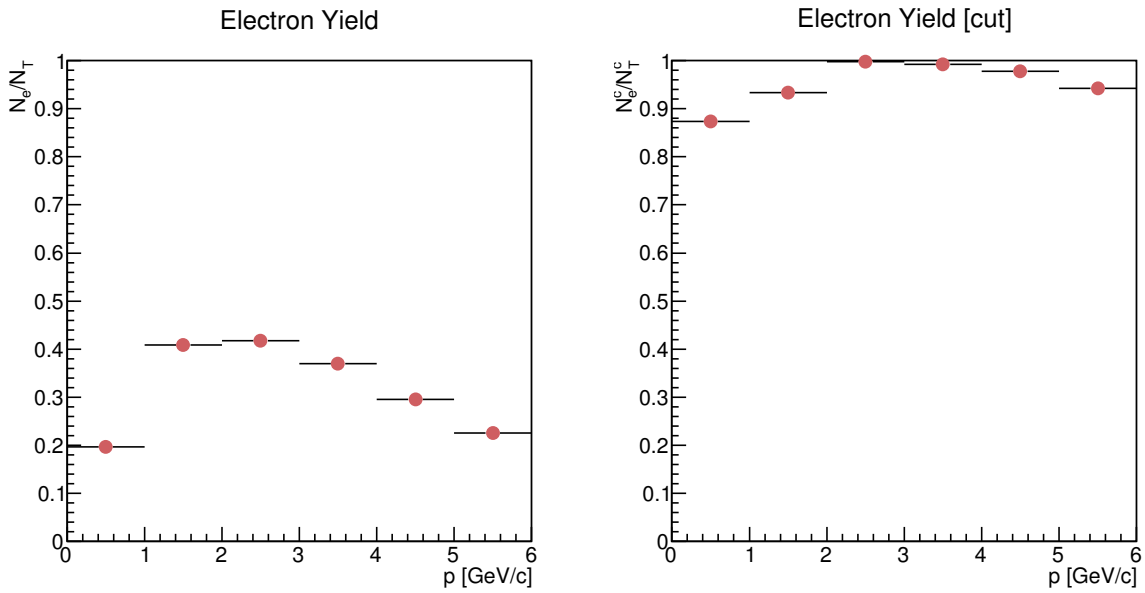

Figure 4.20: Yield of e^- and e^+. These plot on the left depicts the yield before the application of the $\frac{dE}{dx}$ and the $\frac{E}{p}$ cuts, whereas the plot on the right shows the yield after the cuts.

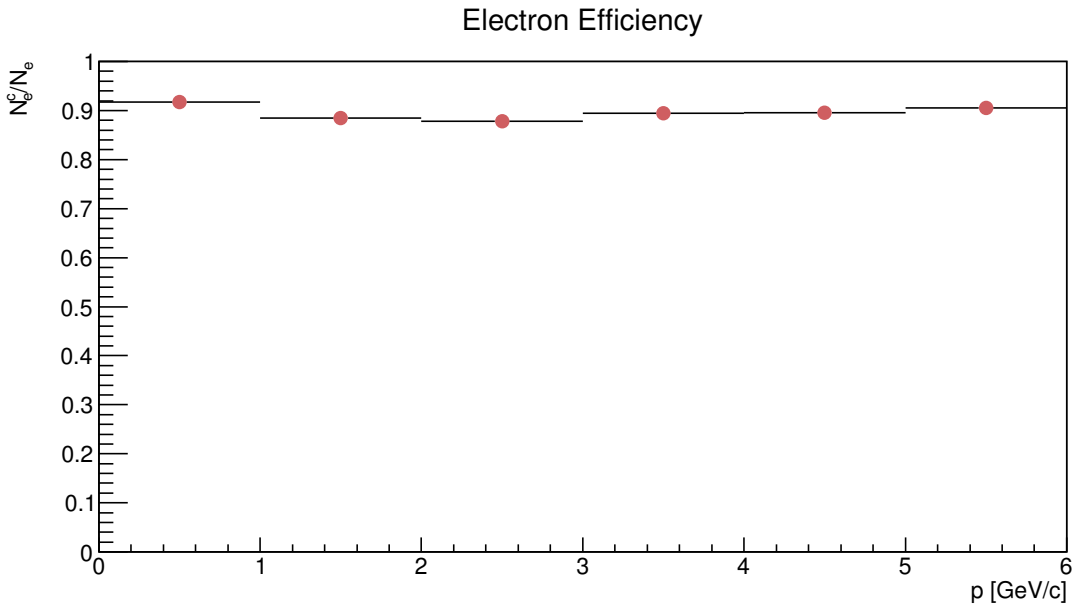

Figure 4.21: Efficiency of the e^- and e^+ after the application of the $\frac{dE}{dx}$ and the $\frac{E}{p}$ cuts, for most $e^\pm$ matched with the EMCal.

A careful analysis of these plots distinctly portrays the improvements in the yield and efficiency of $e^\pm$. If the only particles considered are the ones in the $0.8 \leqslant E/p \leqslant 1.2$ range, then the starting number of $e^\pm$ are higher, as seen in the graph on the left hand side of figure 4.20. By taking a closer look at one of the data points, for the $2 \leqslant p \leqslant 3GeV/c$ range, for example, it is possible to note that the starting number of $e^\pm$ is higher than 40%, compared to less than 10%, as seen in figure 4.18, when the full range of E/p is initially considered. The same tendency can be observed for the efficiency. In this case, the efficiency for every momentum range lies

around 90%, a substantial improvement when compared to the efficiency obtained for the full E/p range (see figure 4.19). In this latter case the efficiency fell below the 40% line for most momentum ranges.

4.6 Application to real data

Using the results obtained in the previous sections as a guideline, that is, using MC simulation data to calculate efficiency, the method of separating $e^{\pm}$ was applied in real data samples, aiming at verifying if reasonable results could be obtained. Naturally, since the real data does not contain the specific particle identity tag, it is not possible to calculate the yield and the efficiency. However, it is possible to obtain the same types of plots that were obtained for the Monte Carlo data. By comparing the general traits of the data and MC plots, it is possible to check if the analytical model developed is, at least qualitatively, compatible when used with different data sets, i.e. simulation and real experimental data. To check the effects that the analytical process of inserting cuts has on real collision data, a plot of loss of energy as a function of traveled distance was obtained as seen in figure 4.22. Observing the plot carefully, the patterns characteristic for each of the individual types of particles can be seen. Aiming at reproducing the same results as with the Monte Carlo data, the data points corresponding to the e^- and e^+ band were segregated from the rest of the events.

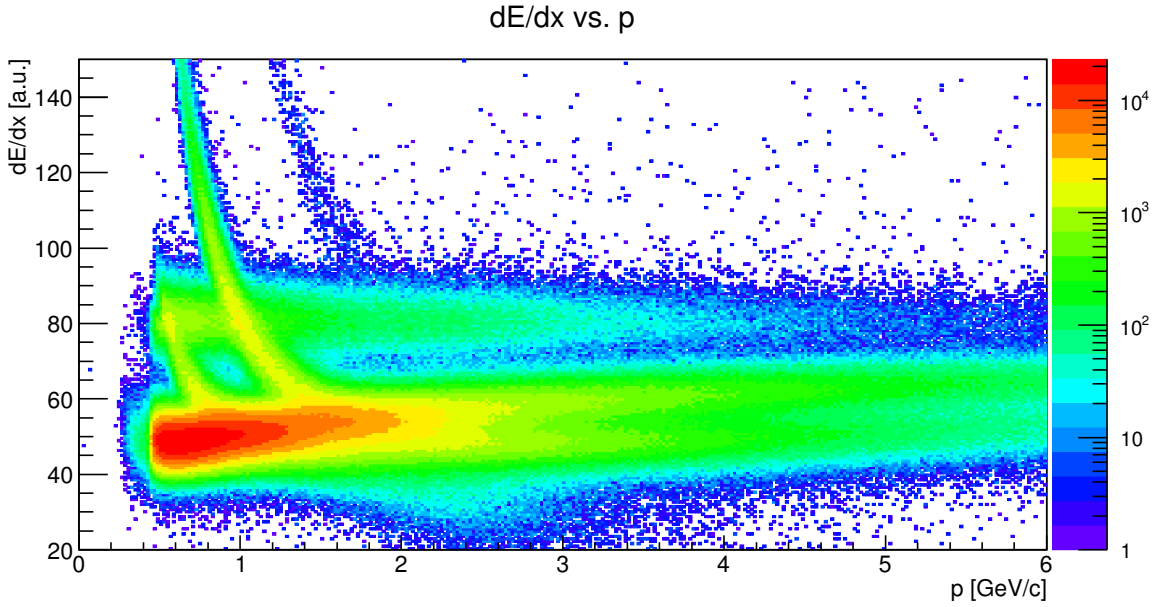

Figure 4.22: Plot of energy loss per distance traveled ($\frac{dE}{dx}$) as a function of total momentum (p), without any cuts applied for the full range of momentum (0 GeV/c to 6 GeV/c). When comparing with figure 4.10, it is possible to observe the same data patterns for the corresponding particles.

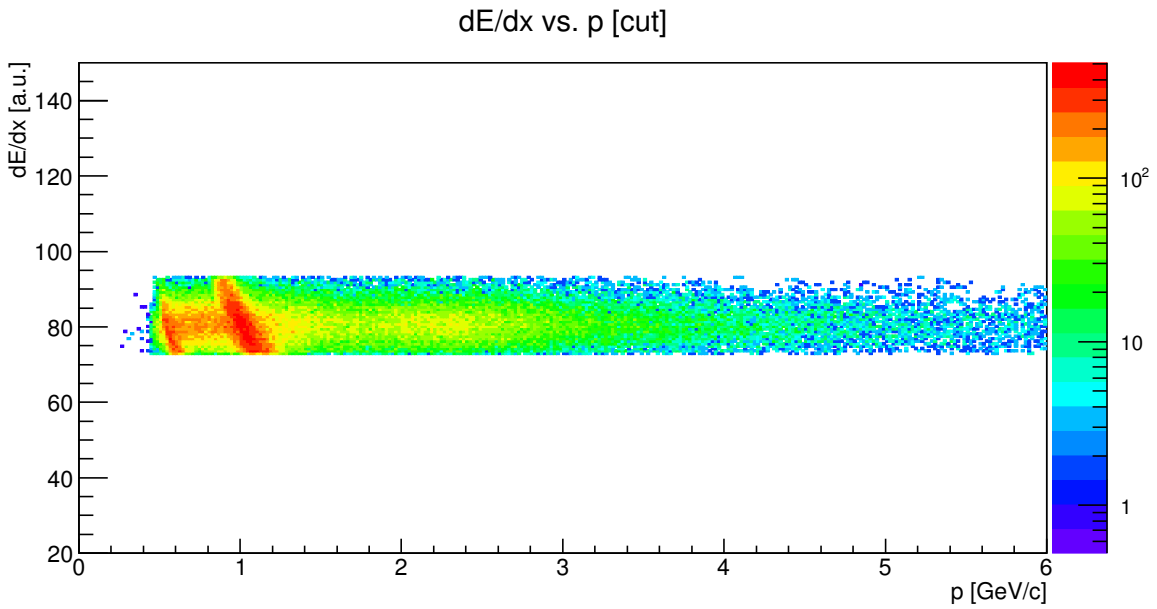

Figure 4.23: Same as figure 4.22, but with cuts applied, i.e. $73a.u. \leqslant \frac{dE}{dx} \leqslant 93a.u.$

An adjustment to the values of the TPC signal had to be made so as to select the correct events associated with e^- and e^+ energy loss. Instead of adopting the TPC signal cut band from 80 to 100a.u., the values that defined the acceptance data band were chosen to be 73 to 93a.u. These specific values for the limits were chosen based on the visual analysis of the $\frac{dE}{dx}$ versus momentum plot shown in figure 4.22. The resulting plot, i.e. after the cut, is depicted in figure 4.23. Again, the plot by itself does not really elucidate what is going on in terms of data selection improvement.

Nevertheless, when looking at the information furnished by the EMCal, namely the total absorbed energy, it is possible to obtain the energy to momentum ratio, E/p, as was done with the MC simulation data. In figure 4.24 it is possible to observe the same two distribution peaks as was observed previously with the MC data set. That is, one centered at $E/p \simeq 0.1$, and the one of interest, corresponding to the electron/positron distribution, centered at $E/p \simeq 1$. And just as done with the simulation data, a cut accepting values of E/p in the range of 0.8 to 1.2 was applied to the data. The results obtained are shown in the graphs of figure 4.25. Based on the yield and efficiency results obtained with the MC simulation data, it is reasonable to assume that this specific data analysis process, that is, the use of cuts for the measure of energy loss in the TPC and the ratio of EMCal energy to momentum, will separate electrons and positrons from the rest of the particles. The number of remaining $e^{\pm}$ left in the sample will be close to 90% from the original number, and there will be a certainty of also close to 90% that the particles will actually be $e^{\pm}$.

Something worth noting in the histograms showing the distribution of the number of oc-

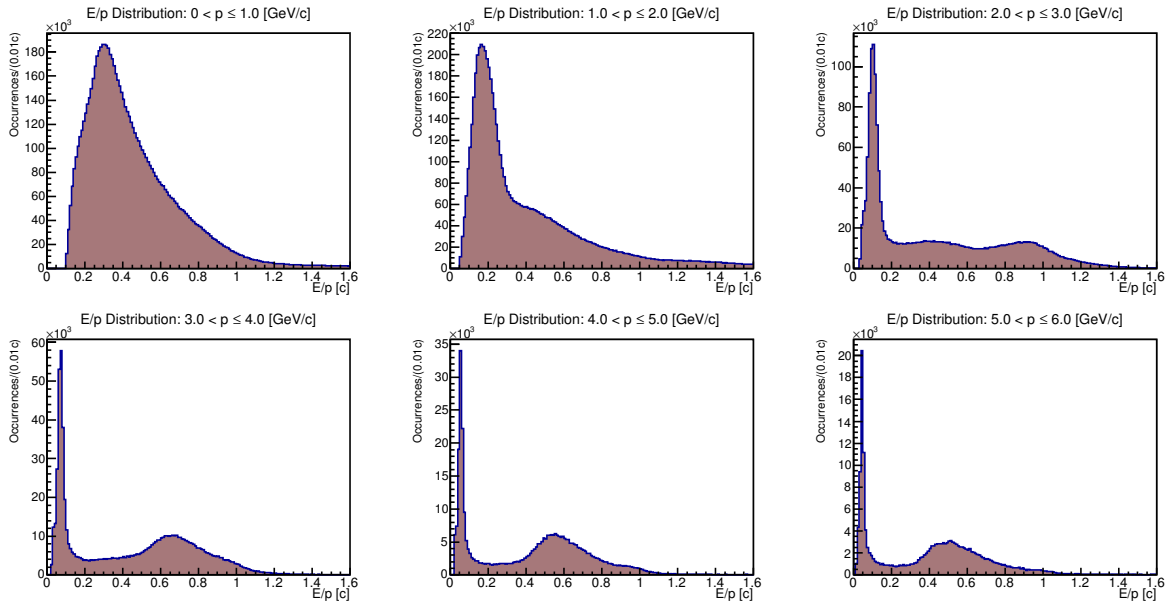

Figure 4.24: Graphs of energy to momentum ratio $\left(\frac{E}{p}\right)$, obtained from the analyzed real collision data. These graphs depict the original data and do not include the results of the application of any cuts.

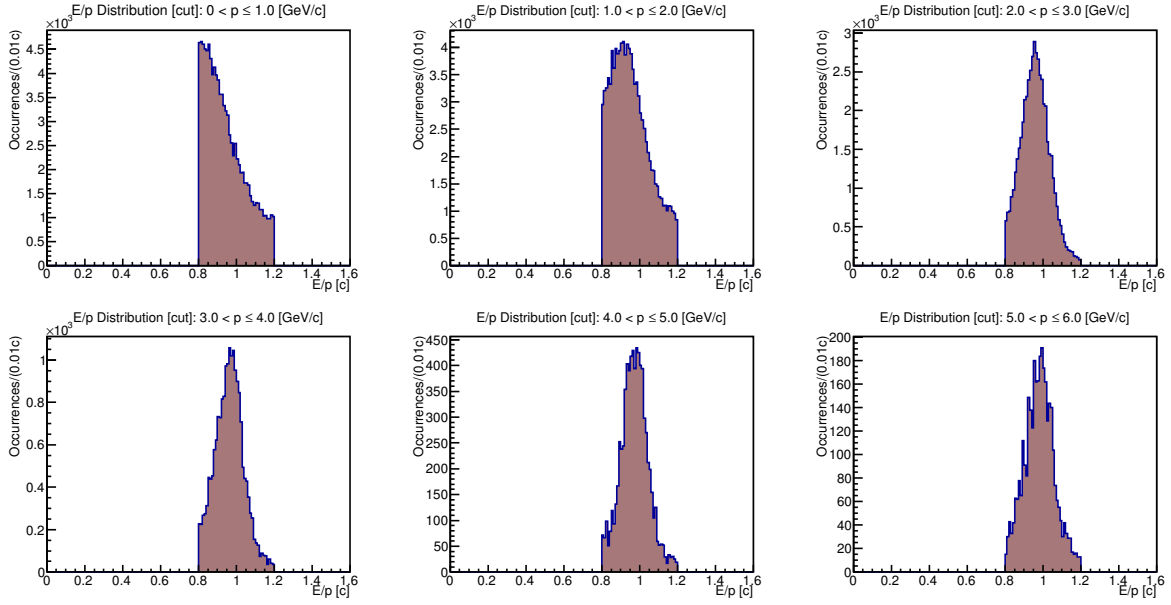

Figure 4.25: Same as figure 4.24, but now showing the results of the $\frac{dE}{dx}$ cut.

currences per E/p, is that for lower momenta, for example, from 0 to 2GeV/c, there is an abrupt, sharp vertical cut on the left side of the distribution. This is fundamentally due to two processes, background contamination of other particles, and Bremsstrahlung effects originated from the emission of electromagnetic radiation from decelerating high energy electrons, when encountering other electrons in the material, thus accounting for path deflection and loss of energy. This phenomenon shifts the centroid of these distributions slightly towards the left of the graph, away from the value one.

5 Conclusions

Having had the opportunity to work with the samples of data collected with the ALICE detectors, i.e. TOF, TPC, and EMCal, it was possible to observe that electrons and positrons emerging from various sorts of decay processes are readily separable using the time projection chamber and the electromagnetic calorimeter detectors. In spite of the fact that electrons and positrons, originated from various distinct sources, were successfully separated from the other types of particles, the research withdrew its source of motivation and incentive from the weak semileptonic decay of heavy flavor, more specifically, from hadronic pp collisions and eventually the subsequent mesonic decays involving Charm and Bottom quarks.

The TOF detector did not separate electrons and positrons from the remaining particles in an efficient manner. There was good separation from Kaons $(K^{\pm})$ and Protons $(p/\bar{p})$ for lower momentum $(|p|)$ values, approximately for $|p| < 2GeV/c$. For momenta above this value, the separation became harder due to the fact that $K^{\pm}$ and $p/\bar{p}$ tend to obtain a β value that approaches the asymptotic value of one $(\beta \to 1)$. A reasonable separation of $e^{\pm}$ from pions $(\pi^{\pm})$ was not feasible due to the fact that both particles lie at, and spread about, the value of $\beta \approx 1$ for basically the full momentum range. The yield of $e^{\pm}$ remained virtually the same before and after the application of the cut in β, accepting values from 0.97 to 1.03. The efficiency dropped significantly to about 45 to 50%, implying that the cut in β reduced significantly the number of $e^{\pm}$ present in the data.

The TPC data analysis of $\frac{dE}{dx}$ showed that the energy loss of $e^{\pm}$ stayed in the arbitrary unit range from $0.08x10^3$ to $0.1x10^3$, regardless of momentum value. For momentum values above $1.5GeV/c$ and below $6.0GeV/c$, the separation of $e^{\pm}$ from $\pi^{\pm}$, $K^{\pm}$, and $p/\bar{p}$ is practically straight forward. However, for values of momentum below $1.5GeV/c$, there is overlapping of the $e^{\pm}$ with pions and kaons, making the isolation of $e^{\pm}$ from the remaining particles quite difficult.

When the EMCal detector is used, combined with the TPC $\frac{dE}{dx}$ data, the isolation of electrons and positrons from the remaining particles is substantially improved. By selecting the

band of the quantity $\frac{E}{|p|}$ centered at one, a substantial improvement in the yield and efficiency calculations are observed. That is, when the values of the ratio of energy to momentum fall within the enclosed band delimited by the lower limiting value of 0.8, and the upper limiting value of 1.2, both quantities, yield and efficiency, are on average over 90% in the full momentum range. Hence, it can be concluded that the electrons/positrons produced by various decay processes can be separated from the common background by applying specific $\frac{dE}{dx}$ cuts in the TPC data and $\frac{E}{|p|}$ in the EMCal readings.

Application of the analytical process described above to real experimental data, yielded very similar results. Patterns in the β versus p_T plots, observed with the Monte Carlo simulation data, were also observed when real data was used. The same observation can be made for the $\frac{dE}{dx}$ versus p_T, both before and after the application of the cuts. The $\frac{E}{|p|}$ histogram distribution, just as noted with the simulation data, was centered at around the value one, corroborating the simulation findings and authenticating the adopted analytic methodology.

Bibliography

[1] BHATTACHARYA, T. et al. *(LANL Collaboration).Recent Results of Lattice QCD Simulations*. July 1994. URL: http://www-physics.mps.ohio-state.edu/~kilcup/erpus/. Accessed on 2017-05-14.

[2] AL-HAYDARI, A. et al. Semileptonic form factors D $\rightarrow \pi$, K and B $\rightarrow \pi, K$ from a fine lattice. *The European Physical Journal A*, v. 43, n. 1, p. 107, 2009.

[3] LENZ, A. *Heavy Flavour Physics and Effective Field Theories - [Lecture Notes]*. Durham, UK: [s.n.], February 2017. URL: https://www.ippp.dur.ac.uk/~lenz/Lecture_Flavour_2017.pdf. Accessed on 2017-05-16.

[4] LIPPMANN, C. Particle identification. *Nuclear Instruments and Methods in Physics Research A: Accelerators, Spectrometers, Detectors and Associated Equipment*, Elsevier, v. 666, p. 148–172, 2012.

[5] FRASS, W.; WALCZAK, R. *Passage of Particles through Matter*. 2009. Michaelmas 2009 - Lecture Notes. URL: http://www.thecolourblue.co.uk/posters/Passage.pdf. Accessed on 2016-03-02.

[6] CERN. *Schematic of ALICE subdetectors*. 2013. URL: http://cerncourier.com/cws/article/cern/53084. Accessed on 2017-01-26.

[7] BOMBONATI, C. et al. Study on impact parameter of charged particles in ALICE - preparing for studying electrons from semi-leptonic heavy-flavor decay at LHC energies. *GSI Scientific Report, NQMA-Experiments-25*, 2009.

[8] GARUTTI, E. *Particle Identification (PID) - distinguishing particle types [Lecture Notes]*. 2012. Deutsches Elektronen-Synchrotron; URL: http://www.desy.de/~garutti/LECTURES/ParticleDetectorSS12/L12_PID.pdf. Accessed on 2017-05-17.

[9] ABELEV, B. et al. (ALICE Collaboration). Technical design report for the upgrade of the ALICE time projection chamber. *CERN-LHCC-2013-020*, n. ALICE TDR 016, 2002.

[10] BETEV, L.; CHOCHULA, P. Definition of the ALICE coordinate system and basic rules for sub-detector components numbering. *ALICE-INT-2003-038*, n. EDMS 406391, 2003.

[11] LIPPMANN, C. *Particle Identification in ALICE: An Extra Boost in QGP Studies*. 2012. Part B: Measuring the Time-Of-Flight (TOF) and Transition Radiation (TRD). URL: http://http://alicematters.web.cern.ch/?q=CL_PID2. Accessed on 2016-04-12.

[12] BRYNGEMARK, L. Charged pion identification at high pT in ALICE using TPC dE/dx. In: ESKOLA, K. et al. (Ed.). *6th. International Workshop on High-pT physics at LHC (HPT 2011), Utrecht, The Netherlands, April 4-7, 2011*. Geneva, Switzerland: CERN-Proceedings-2012-001, 2011. p. 148–152. URL: http://inspirehep.net/record/927004/files/arXiv:1109.1896.pdf. Accessed on 2016-06-08.

[13] ABELEV, B. et al. (ALICE Collaboration). Measurement of electrons from semileptonic heavy-flavor hadron decays in *pp* collisions at $\sqrt{s}$=7 TeV. *Phys. Rev. D*, American Physical Society, v. 86, n. 11, p. 112007, Dec 2012. Disponível em: <http://link.aps.org/doi/10.1103/PhysRevD.86.112007>.

[14] CORTESE, P. et al. (ALICE Collaboration). Addendum to the ALICE technical design report of the time-of-flight system (TOF). *CERN-LHCC-2002-016*, n. Addendum to ALICE TDR 008, 2002.

[15] ADARE, A. et al. (PHENIX Collaboration). Onset of π^0 suppression studied in Cu + Cu collisions at $\sqrt{s_{NN}}$ = 22.4, 62.4, and 200GeV. *Phys. Rev. Lett.*, American Physical Society, v. 101, n. 16, p. 162301, Oct. 2008. URL: `http://link.aps.org/doi/10.1103/PhysRevLett.101.162301`.

[16] ADARE, A. et al. (PHENIX Collaboration). J/ψ production in $\sqrt{s_{NN}}$ = 200GeV Cu + Cu collisions. *Phys. Rev. Lett.*, American Physical Society, v. 101, n. 12, p. 122301, Sep 2008. `http://link.aps.org/doi/10.1103/PhysRevLett.101.122301`.

[17] ADARE, A. et al. (PHENIX Collaboration). System-size dependence of open-heavy-flavor production in nucleus-nucleus collisions at $\sqrt{s_{NN}}$ = 200GeV. *Phys. Rev. C*, American Physical Society, v. 90, n. 3, p. 034903, Sep. 2014. URL: `http://link.aps.org/doi/10.1103/PhysRevC.90.034903`.

[18] OLIVE, K. A. et al. (particle data group) review of particle physics. *Chinese Physics C*, v. 38, p. 090001, 2014.

[19] ARTUSO, M.; BARBERIO, E.; STONE, S. B meson decays. *PMC Physics A*, PhysMath Central - Springer Science+Business Media, v. 3, n. 1, 2009.

[20] POLING, R. A. Heavy quark decays. In: JAROS, J.; PESKIN, M. E. (Ed.). *Proceedings of the XIX International Symposium on Lepton and Photon Interactions at High Energies (LEPTON-PHOTON 99)-eConf 990908*. Stanford, CA - USA: SLAC, 1999. p. 55–82. URL: `http://www.slac.stanford.edu/econf/C990809/docs/poling.pdf`. Accessed on 2017-05-14.

[21] WIEDEMANN, H. *Particle Accelerator Physics*. 3. ed. New York, NY: Springer, 2007.

[22] KLEINKNECHT, K. *Detectors for Particle Radiation*. Cambridge: Cambridge University Press, 1986.

[23] FERNOW, R. C. *Introduction to Experimental Particle Physics*. New York, NY: Cambridge University Press, 1986.

[24] FORSHAW, J. R.; SMITH, A. G. *Dynamics and Relativity*. Chichester, West Sussex: John Wiley & Sons, Ltd., 2009.

[25] PLETTNER, T.; BYER, R. L.; SIEMANN, R. H. The impact of einstein's theory of special relativity on particle accelerators. *Journal of Physics B: Atomic, Molecular and Optical Physics*, v. 38, n. 9, p. S741–S752, 2005.

[26] WOODHOUSE, N. M. J. *Special Relativity*. London, UK: Springer-Verlag Berlin Heidelberg, 2003.

[27] GRUPEN, C.; SHWARTZ, B. A. *Particle Detectors*. New York, NY: Cambridge University Press, 2008.

[28] CARRON, N. J. *An Introduction to the Passage of Energetic Particles through Matter*. New York, NY: Taylor & Francis Group, 2007.

[29] LEO, W. R. *Techniques for Nuclear and Particle Physics Experiments, A How-to Approach*. 2. ed. New York, NY: Springer-Verlag Berlin Heidelberg, 1994.

[30] SITAR, B. et al. *Ionization Measurements in High Energy Physics*. New York, NY: Springer-Verlag Berlin Heidelberg, 1993. (Springer Tracts in Modern Physics, v. 124).

[31] SCHULTZ-COULON, H. C.; STACHEL, J. *The Physics of Particle Detectors - Lecture 2: Interaction of Particles with Matter*. Spring Semester 2010. URL: `http://www.kip.uni-heidelberg.de/~coulon/Lectures/Detectors/Free_PDFs/Lecture2.pdf`. Accessed on 2016-02-28.

[32] ZIEGLER, J. F. The stopping of energetic light ions in elemental matter. *Journal of Applied Physics*, v. 85, n. 3, p. 1249–1272, 1999.

[33] STAPNES, S. Instrumentation for high energy physics. In: ELLIS, N.; FLEISCHER, R. (Ed.). *Proceedings of the 2002 European School of High-Energy Physics (Aug. 25. to Sept. 07, 2002 - Pylos, Greece)*. [S.l.]: CERN Scientific Information Service, 2004. p. 197–228.

[34] TAVERNIER, S. *Experimental Techniques in Nuclear and Particle Physics*. New York, NY: Springer-Verlag Berlin Heidelberg, 2010.

[35] KNOLL, G. F. *Radiation Detection and Measurement*. 3. ed. Hoboken, NJ: John Wiley & Sons, Ltd., 1999.

[36] BIRD, T. An overview of the ALICE experiment. *School of Physics and Astronomy - University of South Hampton*, 2010.

[37] AAMODT, K. et al. (ALICE Collaboration). The ALICE Experiment at the CERN LHC. *Journal of Instrumentation*, v. 3, n. 08, p. S08002, 2008.

[38] SNELLINGS, R. (ALICE Collaboration). Heavy-ion physics at the LHC with ALICE. 34_{th} *SLAC Summer Institute On Particle Physics*, 2006.

[39] GLÄSSEL, R. (ALICE TPC Collaboration). The ALICE TPC - An innovative device for heavy ion collisions at LHC. *Nuclear Instruments and Methods in Physics Research*, A 572, p. 64–66, 2007.

[40] SENYUKOV, S. Open heavy flavour analysis with the ALICE experiment at LHC. In: AYALA, A. et al. (Ed.). *Proceedings, 5th International Workshop on High-p_T physics at LHC: Mexico City, Mexico, September 27-October 1, 2010*. Melville, NY: American Institute of Physics (AIP) Conference Proceedings 1348, 2011. ArXiv:1304.2189v1 [hep-ex].

[41] GUERNANE, R. Heavy flavour production in ALICE. In: *Symposium on Hadron Collider Physics 2006 (HCP 2006)*. Durham, United States: Hyper Article en Ligne (HAL-IN2P3) - Centre pour la Communication Scientifique Directe (CCSD/CNRS), 2006. ALICE, présenté par R. Guernane, à paraître dans les proceedings.

[42] ALESSANDRO, B. et al. (ALICE Collaboration). ALICE: Physics Performance Report, Volume II. *Journal of Physics G: Nuclear and Particle Physics*, v. 32, n. 10, p. 1295, 2006.

[43] BASILE, M. et al. A large-area time-of-flight system for a colliding beam machine. *Nucl. Instrum. Methods*, v. 179, n. CERN-EP-80-118, p. 477–485. 26 p, Jul 1980.

[44] DELLACASA, G. et al. (ALICE Collaboration). ALICE technical design report of the time-of-flight system (TOF). *CERN-LHCC-2000-012*, n. ALICE TDR 008, 2000.

[45] DELLACASA, G. et al. (ALICE Collaboration). ALICE technical design report of the time projection chamber system (TOF). *CERN-LHCC-2000-001*, n. ALICE TDR 007, 2000.

[46] GLUCKSTERN, R. Uncertainties in track momentum and direction, due to multiple scattering and measurement errors. *Nuclear Instruments and Methods*, v. 24, p. 381 – 389, 1963.

[47] BLUM, W.; ROLANDI, L. *Particle Detection with Drift Chambers*. New York, NY: Springer-Verlag Berlin Heidelberg, 1993.

[48] LEHRAUS, I. Progress in particle identification by ionization sampling. *Nuclear Instruments and Methods in Physics Research*, v. 217, n. 1–2, p. 43 – 55, 1983.

[49] ALLISON, W. W. M.; COBB, J. H. Relativistic charged particle identification by energy loss. *Ann. Rev. Nucl. Part. Sci.*, v. 30, p. 253–298, 1980.

[50] CORTESE, P. et al. (ALICE Collaboration). ALICE electromagnetic calorimeter technical design report (EMCal). *CERN-LHCC-2008-014*, n. ALICE TDR 014, 2008.

[51] BRAATEN, E.; JIA, Y.; MEHEN, T. Charm-anticharm asymmetries in photoproduction from heavy-quark recombination. *Phys. Rev. D*, v. 66.

[52] ABEYSEKARA, U. et al. ALICE EMCal Physics Performance Report. 2010. ArXiv:1008.0413.

[53] HEINZ, M. T. (ALICE Collaboration). Heavy flavor measurements using high-p_T electrons in the ALICE EMCal. *Journal of Physics: Conference Series*, v. 230, n. 1, p. 012005, 2010. URL: `http://stacks.iop.org/1742-6596/230/i=1/a=012005`.